LETTER

https://doi.org/10.1038/s41586-018-0788-5

Electric–field–tuned topological phase transition in ultrathin Na_3Bi

James L. Collins[1,2,3], Anton Tadich[3,4], Weikang Wu[5], Lidia C. Gomes[6,7], Joao N. B. Rodrigues[6,8], Chang Liu[1,2,3], Jack Hellerstedt[1,2,9], Hyejin Ryu[10,11], Shujie Tang[10], Sung-Kwan Mo[10], Shaffique Adam[6,12], Shengyuan A. Yang[5,13], Michael S. Fuhrer[1,2,3] & Mark T. Edmonds[1,2,3]*

The electric-field-induced quantum phase transition from topological to conventional insulator has been proposed as the basis of a topological field effect transistor[1–4]. In this scheme, 'on' is the ballistic flow of charge and spin along dissipationless edges of a two-dimensional quantum spin Hall insulator[5–9], and 'off' is produced by applying an electric field that converts the exotic insulator to a conventional insulator with no conductive channels. Such a topological transistor is promising for low-energy logic circuits[4], which would necessitate electric-field-switched materials with conventional and topological bandgaps much greater than the thermal energy at room temperature, substantially greater than proposed so far[6–8]. Topological Dirac semimetals are promising systems in which to look for topological field-effect switching, as they lie at the boundary between conventional and topological phases[3,10–16]. Here we use scanning tunnelling microscopy and spectroscopy and angle-resolved photoelectron spectroscopy to show that mono- and bilayer films of the topological Dirac semimetal[3,17] Na_3Bi are two-dimensional topological insulators with bulk bandgaps greater than 300 millielectronvolts owing to quantum confinement in the absence of electric field. On application of electric field by doping with potassium or by close approach of the scanning tunnelling microscope tip, the Stark effect completely closes the bandgap and re-opens it as a conventional gap of 90 millielectronvolts. The large bandgaps in both the conventional and quantum spin Hall phases, much greater than the thermal energy at room temperature (25 millielectronvolts), suggest that ultrathin Na_3Bi is suitable for room-temperature topological transistor operation.

Two-dimensional quantum spin Hall (QSH) insulators are characterized by an insulating interior with bulk bandgap E_g, and topologically protected conducting edge channels that are robust to backscattering by non-magnetic disorder. The QSH effect was first realized in HgTe quantum wells[5] where the small E_g prevents device applications above cryogenic temperatures. This has led to efforts to find new materials with $E_g \gg 25$ millielectronvolts (meV) for room-temperature topological electronic devices (25 meV is the thermal energy at room temperature). Recent reports of QSH insulators bismuthene on SiC ($E_g \approx 0.8$ eV)[6] and monolayer 1T′-WTe_2 ($E_g \approx 50$ meV)[7] are promising, with the QSH effect measured in monolayer WTe_2 up to[9] 100 K. However, a predicted electric-field effect in WTe_2 has not yet been reported experimentally, and a substantial field effect in atomically two-dimensional (2D) bismuthene is unlikely owing to the completely in-plane structure, which suggests that any Stark effect would most probably be small.

Ultrathin films of topological Dirac semimetals (TDSs) are a promising material class to realize the electric-field-tuned topological phase transition, with such a transition predicted[3] in few-layer films of TDS Na_3Bi and Cd_3As_2. Bulk TDSs are zero-bandgap semimetals with a linear band dispersion in all three dimensions around pairs of Dirac points[10–13], whereas few-layer TDSs are predicted[17] to be non-trivial insulators with bulk bandgaps up to about 300 meV for monolayer Na_3Bi. However, experiments on few-layer TDSs are lacking at present, with only 10–15-nm thin films grown to date[14–16]. To unambiguously demonstrate electric field control over the magnitude, electric field-dependence, and topological nature of the bandgap in ultrathin Na_3Bi, we employ two independent experimental techniques. First, we utilize angle-resolved photoelectron spectroscopy (ARPES) to measure directly the electronic band structure and its modification as a result of doping the surface with potassium (K) to generate an electric field. Second, we use scanning tunnelling spectroscopy (STS), which measures the local density of states (LDOS) as a function of energy, to probe the energy gap directly while varying the tip–sample separation and consequently the induced electric field caused by the potential difference between tip and sample. STS also resolves the topological edge state in Na_3Bi at low electric field, demonstrating the topological nature of this phase. These experimental observations are well supported by density-functional theory (DFT) band structure and edge state calculations with and without electric field.

The unit cell of Na_3Bi contains two stacked triple layers in the z direction, comprising Na and Bi atoms that form a honeycomb structure, with interleaved Na atoms, as shown in the crystal structures of Fig. 1a, b. One triple layer and two stacked triple layers correspond to monolayer (ML) and bilayer (BL) Na_3Bi respectively, as illustrated in Fig. 1b. The symmetry groups of pristine ML and BL Na_3Bi, and the result of including a Na surface vacancy are summarized in Methods and Extended Data Fig. 11. In Fig. 1c, scanning tunnelling microscopy (STM) on few-layer $Na_3Bi(001)$ epitaxial films grown via molecular beam epitaxy (MBE) on Si(111) (see Methods for details) reveals coexisting regions of ML and BL Na_3Bi islands that are atomically flat and up to 40 nm in size, along with small areas of bare substrate. Monolayer regions are identified by an additional 0.22 nm distance to the underlying substrate, due to interfacial spacing or structural relaxation which has been observed previously in other atomically thin materials[18]. Figure 1d shows the overall band structure of few-layer Na_3Bi films along the M–Γ–K surface directions measured with ARPES at $h\nu = 48$ eV, along with the 2D Brillouin zone (Fig. 1d inset). Figure 1e shows the second derivative of the spectra in order to enhance low-intensity features. This has been overlaid with DFT calculations for ML (blue) and BL (green) Na_3Bi showing qualitatively good agreement, consistent with the STM topography which shows coexisting ML and BL regions. Photon-energy dependent ARPES (see Extended Data

[1]School of Physics and Astronomy, Monash University, Clayton, Victoria, Australia. [2]Monash Centre for Atomically Thin Materials, Monash University, Clayton, Victoria, Australia. [3]ARC Centre of Excellence in Future Low-Energy Electronics Technologies, Monash University, Clayton, Victoria, Australia. [4]Australian Synchrotron, Clayton, Victoria, Australia. [5]Research Laboratory for Quantum Materials, Singapore University of Technology and Design, Singapore, Singapore. [6]Department of Physics and Centre for Advanced 2D Materials, National University of Singapore, Singapore, Singapore. [7]National Centre for Supercomputing Applications, University of Illinois at Urbana-Champaign, Champaign, IL, USA. [8]Institute for Condensed Matter Theory and Department of Physics, University of Illinois at Urbana-Champaign, Champaign, IL, USA. [9]Institute of Physics of the Czech Academy of Sciences, Prague, Czech Republic. [10]Advanced Light Source, Lawrence Berkeley National Laboratory, Berkeley, CA, USA. [11]Center for Spintronics, Korea Institute of Science and Technology, Seoul, South Korea. [12]Yale-NUS College, Singapore, Singapore. [13]Centre for Quantum Transport and Thermal Energy Science, School of Physics and Technology, Nanjing Normal University, Nanjing, China. *e-mail: mark.edmonds@monash.edu

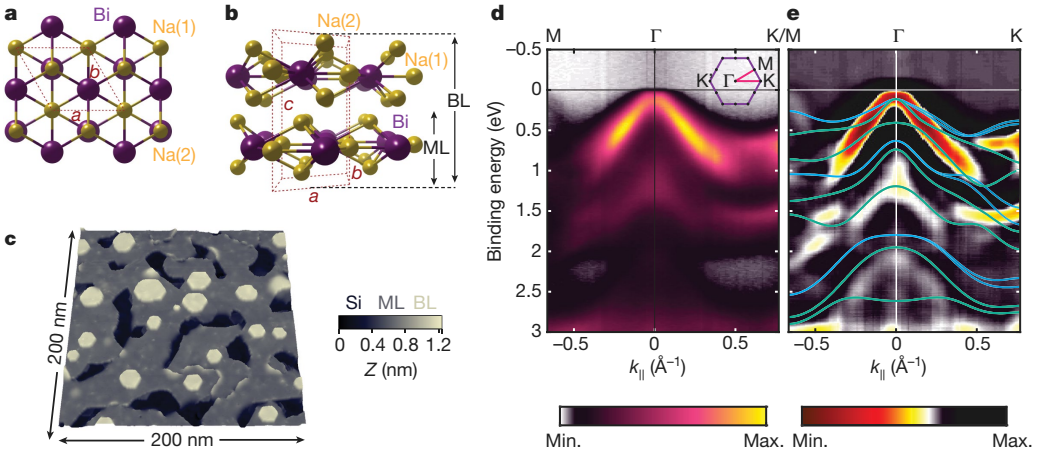

Fig. 1 | Characterization of epitaxial few-layer Na_3Bi and overall electronic structure from ARPES. a, **b**, Top (**a**) and side (**b**) view of the 'bulk' Na_3Bi unit cell with $P6_3/mmc$ symmetry, where $a = b = 0.545$ nm and $c = 0.965$ nm. **c**, Large area (200 nm × 200 nm) topographic STM image (bias voltage $V = 2.0$ V and tunnel current $I = 120$ pA) of few-layer Na_3Bi on Si(111). Regions are colour-coded with ML (monolayer; dark grey), BL (bilayer; light grey) and Si (Si(111); dark blue). **d**, Overall band structure along the M–Γ–K directions measured with ARPES at $h\nu = 48$ eV, with the intensity of emitted photoelectrons, I, reflected in the colour scale. Inset, 2D Brillouin zone. **e**, Second derivative of **d** (see colour scale) enhances low intensity features. Blue and green curves represents DFT band structures for ML and BL Na_3Bi, respectively.

Fig. 2) demonstrates that the film is electronically 2D, with no dispersion in k_z unlike its bulk or 15-nm thin-film counterparts[10,15]. Depth-dependent X-ray photoelectron spectroscopy (XPS; see Extended Data Fig. 1) revealed no additional components observed in either the Si 2*p* core level corresponding to the Si(111) substrate or the Na and Bi core levels of Na_3Bi, verifying that Na_3Bi is free-standing on Si(111).

We first measure the size of the bulk bandgap for ML and BL regions of Na_3Bi by probing the electronic structure with STS, in which the dI/dV spectrum (the differential conductance dI/dV as a function of sample bias V) is proportional to the LDOS at energy $E_F + eV$. Figure 2a shows typical dI/dV spectra for ML (red) and BL (black) with bandgaps corresponding to 0.36 ± 0.025 eV and 0.30 ± 0.025 eV respectively (see Methods for details on extracting bandgap values and discussion on the minimal tip-induced band bending). All dI/dV spectra in Fig. 2a were taken more than 5 nm away from step edges. Figure 2b plots the experimental bandgap (blue squares) in comparison to DFT-calculated values using the generalized gradient approximation (GGA) for pristine Na_3Bi (black circles) and Na_3Bi layers that contain an Na(2) surface vacancy (red circles) (see Methods for details, with associated band structures found in Extended Data Fig. 4). The large bandgap in ML Na_3Bi is consistent with previous calculations[17] and the relatively small change in bandgap from ML to BL observed experimentally is well explained by the DFT calculations that include Na(2) surface vacancies; this vacancy gives rise to a delocalized resonance feature and enhancement of the electronic bandgap[19], resulting in only a small layer-dependent evolution in bandgap. DFT calculations using the GGA method are well known to underestimate the bandgap[20], so we employ the more accurate hybrid functional approach with the modified Becke–Johnson (mBJ) potential to better determine the bandgaps for ML Na_3Bi (without vacancies) (see Methods section 'Experiment parameters' for details). This yields a bandgap of 0.43 eV for ML Na_3Bi, compared to the 0.36 eV obtained for GGA. While the GGA value is in excellent agreement with the experimental value of 0.36 ± 0.025 eV, this is probably a coincidence due to a reduction in the experimental bandgap as a result of the electric field effect modulation discussed later. The zero field value is likely to be larger and closer to the mBJ value.

To verify the prediction that ML and BL Na_3Bi are large-bandgap QSH insulators (see Extended Data Fig. 4) we probe the step edge of these islands to the underlying Si(111) substrate to look for the conductive edge state signature of a QSH insulator. STM topography (Fig. 2c) shows a BL Na_3Bi region decorated with Na surface vacancies and an approximately 1.2 nm step edge to the underlying Si substrate, with a small ML Na_3Bi protrusion about 0.7 nm above the substrate. Figure 2d shows dI/dV spectra for BL Na_3Bi taken 3 nm away from the edge (black curve) and at the edge (blue curve). In contrast to the gap in the bulk, the dI/dV spectrum at the edge is quite different, with states filling the bulk gap along with a characteristic dip at 0 mV bias. Similar features observed in other QSH insulators 1T′-WTe_2 (ref. [7]) and bismuthene[6] have been attributed to one-dimensional (1D) non-trivial edge states and the emergence of a Luttinger liquid[21]. Figure 2e shows dI/dV spectra as a function of distance away from the edge, tracing the orange profile in Fig. 2c, demonstrating the extended nature of the edge state feature, with Fig. 2f showing that the average dI/dV signal within the bulk bandgap moving away from the edge follows the expected exponential decay for a 1D topologically non-trivial state[6].

With ML and BL Na_3Bi verified as large-bandgap QSH insulators, we now examine the role of an electric field in modifying the size and nature of the bandgap. First, we utilize ARPES to measure the band structure after doping the surface with K to generate an electric field. Details on calculating the displacement field are in Methods section 'Mapping from K deposition to electric displacement field'. Figure 3a–d shows the band structure along Γ–K for values of the electric field of 0.0, 0.72, 1.44 and 2.18 V nm^{-1} respectively, with the blue and green/pink dots reflecting the extracted maxima from energy distribution curves (EDC) and momentum distribution curves (MDC; see Methods section 'Extracting and fitting the ARPES band dispersion of few-layer Na_3Bi' for details). The right panel in each pair in Fig. 3a–d represents a model of a 2D gapped Dirac system (see Methods for details). In Fig. 3a only the hole band is observable, with a hyperbolic band dispersion and asymptotic hole Fermi velocity of $v_F \approx 3 \times 10^5$ m s^{-1}. The band dispersion near Γ displays the clear cusp of a band edge indicating a gapped system, with 140 meV separation between the valence band edge and the Fermi energy E_F. The effect of K dosing in Fig. 3b–d is to n-type dope the sample and consequently increase the displacement field. At a displacement field of 0.7 V nm^{-1} the separation from the valence band edge to E_F has increased to about 257 meV. The bandgap must be at least this amount, consistent with STS, though we cannot determine its exact magnitude since the conduction band lies above E_F (although it can be estimated, see Extended Data Fig. 7a). Upon increasing the displacement field, a Dirac-like electron band emerges with asymptotic Fermi velocity $v_F \approx 10^6$ m s^{-1}. The weakness in intensity of the conduction band is most likely due to the different orbital characters of the conduction and valence bands (see Extended Data Figs. 4 and 7 for orbitally resolved DFT band structures). At 1.4 V nm^{-1} our best estimate of the gap between the two band edges is about 100 meV and reduces to

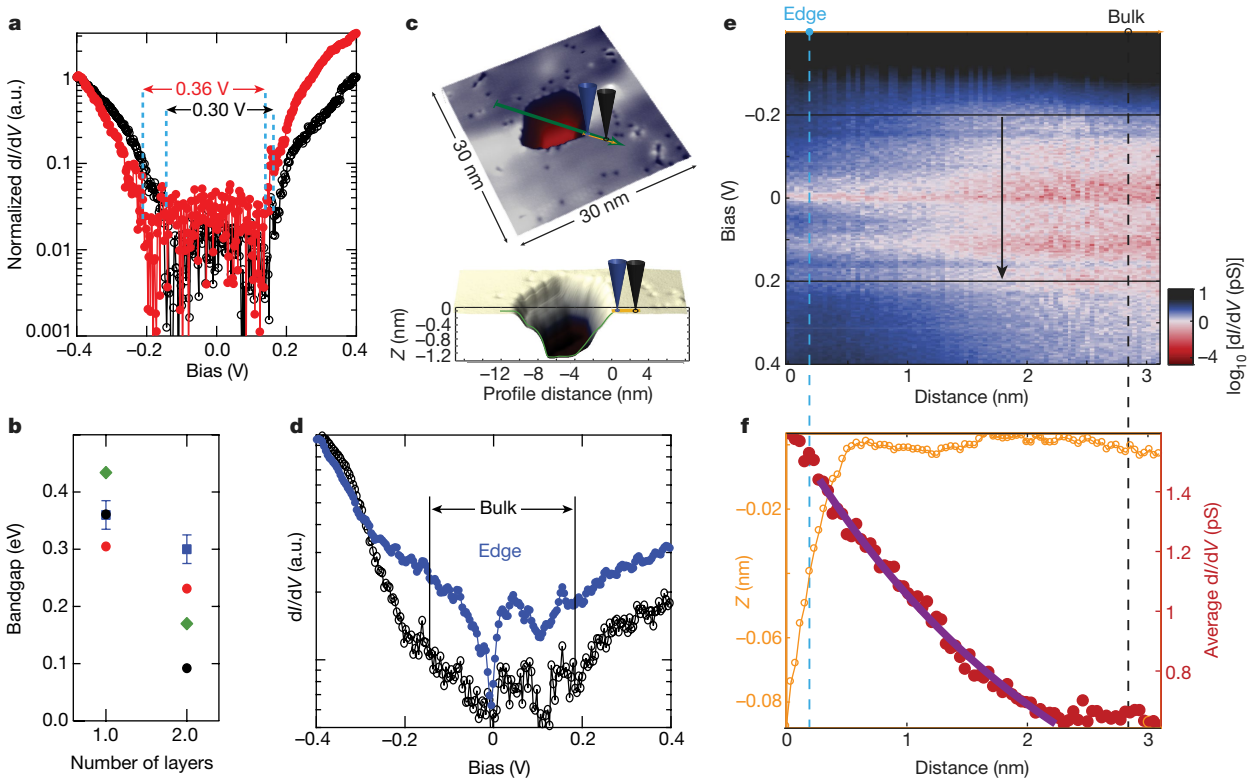

Fig. 2 | Bandgap in ML and BL Na_3Bi and edge state behaviour. **a**, Normalized dI/dV spectra corresponding to ML (red) and BL (black) Na_3Bi. a.u., arbitrary units. Conduction and valence band edges are reflected by the sharp onset of dI/dV intensity, marked by dashed blue lines, separated by 0.36 V (ML) and 0.30 V (BL). **b**, Evolution of the bandgap as a function of layer thickness ('number of layers') determined from dI/dV spectra (blue squares, with error bars of ±25 meV; see Methods for error calculation), DFT calculations using the GGA functional on pristine Na_3Bi (black circles) and with an Na(2) vacancy (red circles), and DFT calculations using the mBJ potential (green diamonds). **c**, Top, STM topography of a region of BL Na_3Bi (grey), and the underlying Si(111) substrate (red). The orange line reflects the region over which the dI/dV measurements were performed in **e**, and the green line extends the profile across the pinhole step. Bottom, cross-section through the pinhole overlaid with the orange and green line profiles. **d**, dI/dV spectra taken near the step edge of BL Na_3Bi to Si(111) substrate (blue) and in the bulk of BL Na_3Bi (black). **e**, dI/dV colour map (scale at bottom right) taken at and then moving away from the step edge where the dashed vertical lines reflect the spectra shown in **d** and the horizontal lines represent the region over which the dI/dV signal was averaged as shown in **f**. **f**, Corresponding intensity profile of dI/dV in the bulk gap showing the exponential decay away from the step edge, where the orange trace represents the topographic height, Z, and the red points are the average dI/dV magnitude within the bulk bandgap (horizontal dashed region of **e**) fitted to an exponential (thick purple line).

about 90 meV at 2.2 V nm^{-1} (see Methods section 'Electric displacement field dependence from ARPES' for calculation). While a significant reduction in bandgap with displacement field clearly occurs, due to the finite energy width of the bands (approximately 100 meV) we cannot say definitively whether the gap is fully closed or even reopened again.

To elucidate the effect of an electric field on the electronic structure more clearly, we turn back to measurements made with STM. Here, the

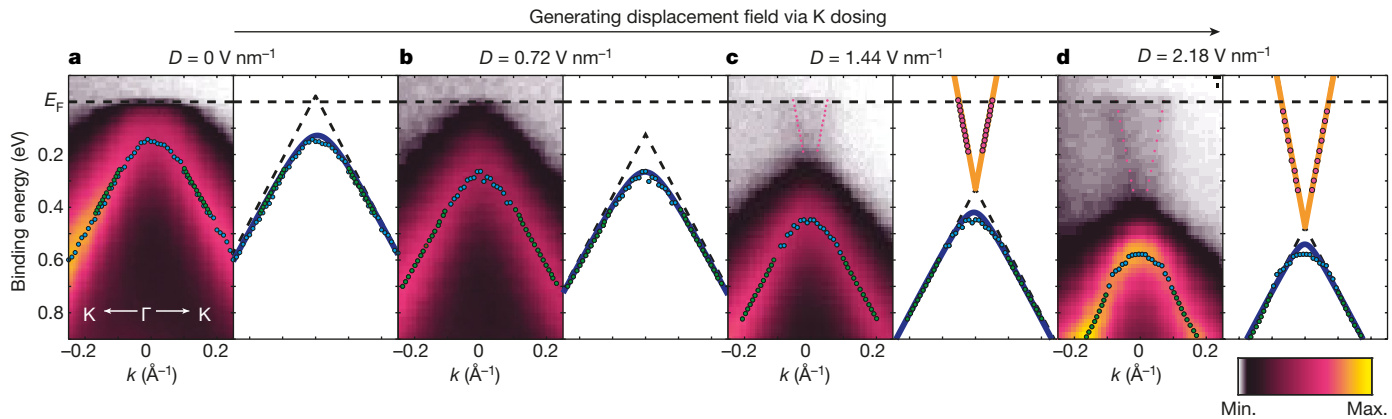

Fig. 3 | Band-structure modulation in ARPES in ML and BL Na_3Bi using potassium (K) dosing. a–d, ARPES intensity plots of the band dispersion with K dosing. For each K dose, the left panel shows the ARPES spectra, points are maxima extracted from MDCs (green/pink) and EDCs (blue); right panel shows fits of the maxima to hyperbolas (orange and blue solid lines represent fits of the conduction and valence bands, respectively) along with linear asymptotes (black dashed lines). **a**, Before K dosing, the hole band is located about 140 meV below E_F; **b**, after the first K dose, at 0.72 V nm^{-1} displacement field, the hole band is 257 meV below E_F; **c**, after the second dose, at 1.44 V nm^{-1} displacement field, the electron band is separated from the hole band by about 100 meV; and **d**, after the last dose, at 2.18 V nm^{-1} displacement field the band separation is 90 meV.

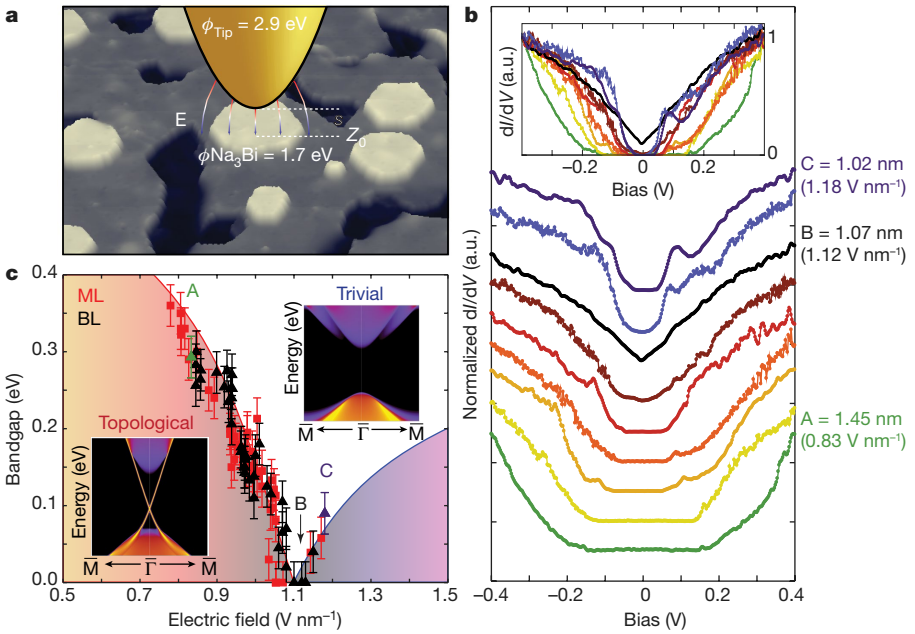

Fig. 4 | Electric-field-induced bandgap modulation of ML and BL Na_3Bi in STM. a, Schematic of a metallic tip at distance *s* above the surface (z_0) of Na_3Bi, with the difference in work function ($\phi_{Tip} - \phi_{Na_3Bi}$) generating a localized electric field (*E*). **b**, Individual d*I*/d*V* spectra taken on BL Na_3Bi at different tip–sample separations (electric fields) as labelled on the figure, where A, B and C correspond to tip heights (electric fields) of 1.45 nm (0.83 V nm^{-1}), 1.07 nm (1.12 V nm^{-1}) and 1.02 nm (1.18 V nm^{-1}), respectively. Spectra have been normalized and offset for clarity. Inset shows the spectra without an offset. **c**, Bandgap extracted from d*I*/d*V* spectra as a function of electric field for ML (red squares) and BL (black triangles) Na_3Bi, with error bars of ±25 meV; see Methods for error calculation. Marked field strengths A, B and C correspond to those indicated in **b**. Orange and purple shaded regions represent guides to the eye. Insets represent DFT projected edge state band structures below and above the critical field, where the colour represents the spectra weight.

tip–sample separation is now varied in order to tune the electric field due to the electrostatic potential difference between the metallic tip and Na_3Bi, as illustrated schematically in Fig. 4a. The electrostatic potential difference is dominated by the difference in work function between the tip and the sample, approximately 1.2 eV (see Methods section 'Calculating tip–sample separation and electric field' for calculation). Changes in the bandgap can then be measured in the d*I*/d*V* spectra as a function of tip–sample separation and converted to electric field as shown in Fig. 4b (details in Methods). Figure 4b shows normalized d*I*/d*V* spectra taken on BL Na_3Bi that are offset for clarity (Extended Data Fig. 9 shows similar spectra taken on ML Na_3Bi) at various tip–sample separations (electric fields). A large modulation occurs upon increasing the electric field strength, with the bandgap reducing from 300 meV to completely closed (and exhibiting the characteristic V-shape of a Dirac semimetal) at about 1.1 V nm^{-1} and then reopening above this to yield a bandgap of about 90 meV at approximately 1.2 V nm^{-1}. Figure 4b inset shows the d*I*/d*V* spectra without any offset, highlighting the clear non-zero density of states at the minimum in conductance (that is, the Dirac point) when the bandgap is closed. Figure 4c plots the bandgap as a function of electric field for ML and BL Na_3Bi, with both exhibiting a similar critical field where the bandgap is closed and then reopened into the trivial/conventional regime with increasing electric field. DFT calculations also predict such a transition, arising from a Stark-effect-induced rearrangement of *s*- and *p*-like bands near the gap (see Methods section 'DFT calculations of electric-field-induced topological phase transition' and Extended Data Fig. 10 for full calculation). The projected edge state band structures above and below the critical field are shown as insets to Fig. 4c. Note that due to the difficulty of estimating tip–sample distance, the electric field magnitude may include a systematic error as large as 50%, however the trend of gap size with electric field is correct (see Methods for detailed discussion).

By combining ARPES and STS, we have demonstrated that ML and BL Na_3Bi are QSH insulators with bulk bandgaps above 300 meV, offering the potential to support dissipationless transport of charge at room temperature. An electric field tunes the phase from topological insulator to conventional insulator with a bandgap of about 90 meV due to a Stark-effect-driven transition. This bandgap modulation of more than 400 meV is larger than has been achieved in atomically thin semiconductors such as bilayer graphene[22,23], is similar to that achieved in phosphorene[24], and may be useful in optoelectronic applications[25] in the mid-infrared. Na_3Bi is chemically inert in contact with silicon, and the electric fields required to induce the topological phase transition are below the breakdown fields of conventional dielectrics, meaning that future experiments that measure the ballistic edge current turn on/turn off along the film edges may be possible. These properties make ultrathin Na_3Bi a promising platform for realizing new forms of electronic switches based on topological transistors for low-energy logic circuits.

Online content

Any methods, additional references, Nature Research reporting summaries, source data, statements of data availability and associated accession codes are available at https://doi.org/10.1038/s41586-018-0788-5.

Received: 1 March 2018; Accepted: 7 October 2018;
Published online: 10 December 2018

1. Qian, X., Liu, J., Fu, L. & Li, J. Quantum spin Hall effect in two-dimensional transition metal dichalcogenides. *Science* **346**, 1344–1347 (2014).
2. Liu, J. et al. Spin-filtered edge states with an electrically tunable gap in a two-dimensional topological crystalline insulator. *Nat. Mater.* **13**, 178–183 (2014).
3. Pan, H., Wu, M., Liu, Y. & Yang, S. A. Electric control of topological phase transitions in Dirac semimetal thin films. *Sci. Rep.* **5**, 14639 (2015).
4. Vandenberghe, W. G. & Fischetti, M. V. Imperfect two-dimensional topological insulator field-effect transistors. *Nat. Commun.* **8**, 14184 (2017).
5. König, M. et al. Quantum spin Hall insulator state in HgTe quantum wells. *Science* **318**, 766–770 (2007).
6. Reis, F. et al. Bismuthene on a SiC substrate: a candidate for a high-temperature quantum spin Hall material. *Science* **357**, 287–290 (2017).
7. Tang, S. et al. Quantum spin Hall state in monolayer 1T′-WTe_2. *Nat. Phys.* **13**, 683–687 (2017).
8. Fei, Z. et al. Edge conduction in monolayer WTe_2. *Nat. Phys.* **13**, 677–682 (2017).

9. Wu, S. et al. Observation of the quantum spin Hall effect up to 100 kelvin in a monolayer crystal. *Science* **359**, 76–79 (2018).
10. Liu, Z. K. et al. Discovery of a three-dimensional topological Dirac semimetal, Na_3Bi. *Science* **343**, 864–867 (2014).
11. Wang, Z. et al. Dirac semimetal and topological phase transitions in A_3Bi (A=Na, K, Rb). *Phys. Rev. B* **85**, 195320 (2012).
12. Liu, Z. K. et al. A stable three-dimensional topological Dirac semimetal Cd_3As_2. *Nat. Mater*. **13**, 677–681 (2014).
13. Borisenko, S. et al. Experimental realization of a three-dimensional Dirac semimetal. *Phys. Rev. Lett.* **113**, 027603 (2014).
14. Hellerstedt, J. et al. Electronic properties of high-quality epitaxial topological Dirac semimetal thin films. *Nano Lett.* **16**, 3210–3214 (2016).
15. Zhang, Y. et al. Molecular beam epitaxial growth of a three-dimensional topological Dirac semimetal Na_3Bi. *Appl. Phys. Lett.* **105**, 031901 (2014).
16. Schumann, T. et al. Observation of the quantum Hall effect in confined films of the three-dimensional Dirac semimetal Cd_3As_2. *Phys. Rev. Lett.* **120**, 016801 (2018).
17. Niu, C. et al. Robust dual topological character with spin-valley polarization in a monolayer of the Dirac semimetal Na_3Bi. *Phys. Rev. B* **95**, 075404 (2017).
18. Wu, J. et al. High electron mobility and quantum oscillations in non-encapsulated ultrathin semiconducting Bi_2O_2Se. *Nat. Nanotechnol*. **12**, 530–534 (2017).
19. Edmonds, M. T. et al. Spatial charge inhomogeneity and defect states in topological Dirac semimetal thin films of Na_3Bi. *Sci. Adv*. **3**, eaao6661 (2017).
20. Perdew, J. P. et al. Understanding band gaps of solids in generalized Kohn-Sham theory. *Proc. Natl Acad. Sci. USA* **114**, 2801–2806 (2017).
21. Voit, J. One-dimensional Fermi liquids. *Rep. Prog. Phys*. **58**, 977–1116 (1995).
22. Ohta, T., Bostwick, A., Seyller, T., Horn, K. & Rotenberg, E. Controlling the electronic structure of bilayer graphene. *Science* **313**, 951–954 (2006).
23. Zhang, Y. et al. Direct observation of a widely tunable bandgap in bilayer graphene. *Nature* **459**, 820–823 (2009).
24. Deng, B. et al. Efficient electrical control of thin-film black phosphorus bandgap. *Nat. Commun*. **8**, 14474 (2017).
25. Ju, L. et al. Tunable excitons in bilayer graphene. *Science* **358**, 907–910 (2017).

Acknowledgements M.T.E. was supported by ARC DECRA fellowship DE160101157. M.T.E., J.L.C., C.L. and M.S.F. acknowledge funding support from CE170100039. J.L.C., J.H. and M.S.F. are supported by M.S.F.'s ARC Laureate Fellowship (FL120100038). S.A. acknowledges funding support from ARC Discovery Project DP150103837. M.T.E. and A.T. acknowledge travel funding provided by the International Synchrotron Access Program (ISAP) managed by the Australian Synchrotron, part of ANSTO, and funded by the Australian Government. M.T.E. acknowledges funding from the Monash Centre for Atomically Thin Materials Research and Equipment Scheme. S.A.Y. and W.W. acknowledge funding from Singapore MOE AcRF Tier 2 (grant no. MOE2015-T2-2-144). S.A. acknowledges the National University of Singapore Young Investigator Award (R-607-000-094-133). This research used resources of the Advanced Light Source, which is a DOE Office of Science User Facility under contract no. DE-AC02-05CH11231. Part of this research was undertaken on the soft X-ray beamline at the Australian Synchrotron, part of ANSTO. The authors acknowledge computational support from the National Supercomputing Centre, Singapore.

Author contributions M.T.E., J.L.C. and M.S.F. devised the STM experiments. M.T.E. devised the ARPES and XPS experiments. M.T.E. and J.L.C. performed the MBE growth and STM/STS measurements at Monash University. J.H. assisted with the experimental setup at Monash University. M.T.E., J.L.C. and A.T. performed the MBE growth and ARPES measurements at Advanced Light Source with the support from H.R., S.T. and S.-K.M. The MBE growth and XPS measurements at the Australian Synchrotron were performed by M.T.E., J.L.C., A.T., J.H. and C.L. The DFT calculations were performed by L.C.G., J.N.B.R., W.W. and S.A.Y.; S.A. assisted with the theoretical interpretation of the data. M.T.E., J.L.C. and M.S.F. composed the manuscript. All authors read and contributed feedback to the manuscript.

Competing interests The authors declare no competing interests.

Additional information
Extended data is available for this paper at https://doi.org/10.1038/s41586-018-0788-5.
Reprints and permissions information is available at http://www.nature.com/reprints.
Correspondence and requests for materials should be addressed to M.T.E.
Publisher's note: Springer Nature remains neutral with regard to jurisdictional claims in published maps and institutional affiliations.

METHODS

Growth of few-layer Na_3Bi on Si(111). Ultrathin Na_3Bi thin films were grown in ultrahigh vacuum (UHV) molecular beam epitaxy (MBE) chambers and then immediately transferred after the growth under UHV to the interconnected measurement chamber (that is, Createc LT-STM at Monash University, Scienta R-4000 analyser at Advanced Light Source and SPEC Phoibos 150 at Australian Synchrotron). To prepare an atomically flat substrate, a p-type Si(111) wafer was flash annealed to 1,250 °C in order to achieve a (7×7) surface reconstruction (this was achieved via direct current heating at Monash University and the Australian Synchrotron, and via electron bombardment heating at the Advanced Light Source).

For Na_3Bi film growth, effusion cells were used to simultaneously evaporate elemental Bi (99.999%) in an overflux of Na (99.95%) with a Bi:Na flux ratio not less than 1:10, calibrated by quartz microbalance. During growth, the substrate temperature was held between 300 °C and 330 °C to ensure successful crystallization. At the end of the growth, the sample was left at the growth temperature for 10 min in a Na overflux to improve film quality before cooling to room temperature.

Experiment parameters. *STM/STS measurements.* These were performed in a Createc LT-STM operating at 5 K. A PtIr tip was prepared and calibrated using an Au(111) single crystal, confirming the presence of the Shockley surface state at −0.5 V and flat LDOS near the Fermi level before all measurements. After measurements on few-layer Na_3Bi were completed, the Au(111) sample was re-measured to confirm the tip had not significantly changed and still exhibited flat LDOS near the Fermi level. STM differential conductance measurements (dI/dV) were measured using a 5 mV AC excitation voltage (673 Hz) that was added to the tunnelling bias. Differential conductance measurements were made under open feedback conditions with the tip in a fixed position above the surface. Data were prepared and analysed using MATLAB and IGOR Pro.

ARPES measurements. These were performed at Beamline 10.0.1 of the Advanced Light Source (ALS) at Lawrence Berkeley National Laboratory, USA. Data were taken using a Scienta R4000 analyser at 20 K sample temperature. The total energy resolution was 20–25 meV depending on the beamline slit widths and analyser settings, and the angular resolution was 0.2°. This resulted in an overall momentum resolution of ~0.01 $Å^{-1}$ for photoelectron kinetic energies measured, with the majority of the measurements performed at $h\nu = 48$ eV and 55 eV. Doping of the Na_3Bi films was performed via in situ K dosing from a SAES getter source in UHV. Dosing was performed at a temperature of 20 K to avoid K clustering.

XPS measurements. These were performed at the Soft X-ray Beamline of the Australian Synchrotron using a SPECS Phoibos-150 spectrometer at room temperature. The Bi 5*d* and Na 2*p* of the Na_3Bi, as well as the Si 2*p* of the Si(111) substrate, were measured at photon energies of 100 eV, 350 eV, 800 eV and 1,487 eV. This ensured surface sensitivity for the low photon energy scans at 100 eV, with the higher photon energies used to characterize the depth dependence of the core levels, in particular whether there was any chemical bonding between the Na_3Bi film and the Si(111) substrate. The binding energy scale of all spectra are referenced to the Fermi energy (E_F), determined using either the Fermi edge or 4*f* core level of an Au reference foil in electrical contact with the sample. Core level spectra were analysed using a Shirley background subtraction. Kelvin probe measurements to determine the work function of Na_3Bi were also performed on this system.

Density-functional theory calculations. First-principles calculations based on density-functional theory (DFT) were used to obtain electronic band structures of monolayer (ML) and bilayer (BL) Na_3Bi, with and without Na(2) vacancies. This was achieved using the projector augmented wave (PAW) method[26] with calculations implemented in Quantum ESPRESSO code and the Vienna *ab initio* Simulation Package (VASP). The generalized gradient approximation (GGA) using the Perdew–Burke–Ernzerhof (PBE) functional[27] for the exchange-correlation potential was adopted. The plane-wave cutoff energy was set to be 400 eV. The Brillouin zone sampling was performed by using *k* grids with a spacing of $2\pi \times 0.02$ $Å^{-1}$ within a Γ-centred sampling scheme. For all calculations, the energy and force convergence criteria were set to be 10^{-5} eV and 10^{-2} eV $Å^{-1}$, respectively. For the ML and BL Na_3Bi calculations with Na surface vacancies there is 1 Na vacancy per 2×2 supercell. For the Na_3Bi layers, we used a vacuum region of thickness greater than 15 Å to eliminate the artificial interaction between the periodic images. The edge states were studied by constructing the maximally localized Wannier functions[28] and by using the iterative Green's function method[29] as implemented in the WannierTools package[30]. More accurate calculations of the bandgap for ML and BL Na_3Bi (without Na vacancies) were performed via a more accurate hybrid functional approach using the modified Becke–Johnson potential[31–33].

Characterization via RHEED, LEED and XPS. In order to confirm that the few-layer films of Na_3Bi are high quality and epitaxial over large areas, we performed reflection high-energy electron diffraction (RHEED), low energy electron diffraction (LEED) and X-ray photoelectron spectroscopy (XPS), as shown in Extended Data Fig. 1. Extended Data Fig. 1a shows the characteristic RHEED pattern for Si(111) 7×7 reconstruction along $\bar{\Gamma}-\bar{M}$, while Extended Data Fig. 1b shows the RHEED pattern for few-layer Na_3Bi along $\bar{\Gamma}-\bar{K}$, consistent with RHEED reported on films of 15 unit cell thickness, where the lattice orientation of Na_3Bi is rotated 30° with respect to the Si(111) substrate[15]. Extended Data Fig. 1c shows the 1×1 LEED pattern consistent with growth of Na_3Bi in the (001) direction. The sharpness of the spots and the absence of rotational domains indicates high-quality single crystal few-layer Na_3Bi over a large area. Extended Data Fig. 1d shows the Bi 5*d* and Na 2*p* core levels of a few-layer Na_3Bi film taken at $h\nu = 100$ eV, with the peak positions consistent with published results on 20 nm film and bulk Na_3Bi[10,15,34].

To rule out reaction of Na_3Bi with the Si substrate, we performed depth-dependent XPS (by varying the photon energy in order to increase the kinetic energy of emitted photoelectrons, as a result increasing the mean free path) to examine the Na_3Bi–Si(111) interface. The Na and Bi core levels exhibited no additional components (data not shown). Extended Data Fig. 1e shows XPS of the Si 2*p* core level (reflecting the substrate) at photon energy $h\nu = 350$ eV (left panel) and $h\nu = 850$ eV (right panel). In each panel the black curve represents the Si 2*p* core level of the bare Si(111) 7×7 and the red curve represents the Si 2*p* core level with few-layer Na_3Bi grown on top. In each case, the spectra have been normalized to the maximum in intensity and energy-corrected (to account for the small interfacial charge transfer that occurs) in order to overlay the core levels. The spectra have been offset for clarity. It is clear there is negligible change to the Si 2*p* core level after Na_3Bi growth, with no additional components or significant broadening arising, verifying that Na_3Bi is free-standing on Si(111). This is consistent with the fact that our ARPES measurements on ultrathin Na_3Bi showed no features with the Si(111) 7×7 symmetry.

Band dispersion in k_z from photon-energy-dependent ARPES. Photon energy-dependent ARPES can be used to determine whether a material possesses a 3D band dispersion, that is, the binding energy E_B depends not only on in-plane wavevectors k_x and k_y, but also on out-of-plane wavevector k_z. To determine the momentum perpendicular to the surface requires measuring energy distribution curves as a function of the photon energy in order to measure E_B versus k_z, using the nearly free-electron final state approximation[35,36]:

$$k_z = \sqrt{\frac{2m}{\hbar^2}(E_k + V_0 - E_k \sin^2\theta)} \quad (1)$$

where θ is the emission angle, m is the effective mass of an electron, V_0 is the inner potential (reflecting the energy difference between the bottom of the valence band and the vacuum level) and E_k is the kinetic energy of the emitted photoelectrons (where $E_k = h\nu - \Phi - E_B$, with $h\nu$ the photon energy, Φ the work function and E_B the energy). At normal emission (that is, $\theta = 0$), equation (1) simplifies to:

$$k_z = \sqrt{\frac{2m}{\hbar^2}(E_k + V_0)} \quad (2)$$

Therefore, using equation (2) and measuring energy distribution curves at normal emission as a function of photon energy, we can directly measure E_B versus k_z assuming an inner potential $V_0 = 12.5$ eV for Na_3Bi determined in ref. [10].

Extended Data Fig. 2 shows a colour plot of k_z as a function of binding energy (and reflects energy distribution curves taken at normal emission for photon energies between 45 eV and 55 eV. A flat band is observed near 0 eV (the Fermi energy) and represents the valence band maximum. This band possesses no dispersion in k_z (that is, no bulk band dispersion), verifying that few-layer Na_3Bi is indeed electronically 2D, unlike its thin-film and bulk counterparts.

Bandgap extraction from STM spectra. Determining the bulk electronic bandgap of ML and BL Na_3Bi was achieved by performing scanning tunnelling spectroscopy (dI/dV as a function of sample bias V) more than 5 nm away from step edges. The valence and conduction band edges in the LDOS are defined as the onset of differential conductance intensity above the noise floor. Owing to the large variation in dI/dV signal near a band edge, it is difficult to determine the bandgap on a linear scale as shown in Extended Data Fig. 3a, and it is therefore useful to plot the logarithm of the dI/dV curves for accurate bandgap determination, as shown in Extended Data Fig. 3b.

For measurements involving tuning the electric field by varying the tip–sample distance, dI/dV spectra were taken over a wide range of tunnelling currents (0.01–1 nA), resulting in large changes in signal at band edges and a change in the relative magnitude of signal to noise. In order to unambiguously determine the magnitude of the gap without reference to the noise magnitude, we adopted the following procedure. Spectra were normalized to a relatively featureless point in the LDOS away from the band edge onset. The dI/dV signal corresponding to a bias of −400 meV was chosen for normalization. After the normalization procedure was completed for all spectra, we take the band edges as the point at which the dI/dV has fallen to 0.01 of the normalized value. We find that this definition closely corresponds to the onset of conductance above the noise floor (Extended Data Fig. 3c). Normalization was also performed at −300 meV, 300 meV and 400 meV with only a small variation (<15 meV) observed, due to the sharp onset

in conductance in both the valence and conduction bands. Accounting for error in the normalization and the tip-induced band bending discussed below yields an error in determining the gap magnitude of ±25 meV.

Tip-induced band bending. Tip-induced band bending (TIBB) effects have the potential to overestimate the size of the electronic bandgap due to unscreened electric fields and can strongly influence the interpretation of STM data. The absence/presence of TIBB is usually verified by performing dI/dV spectra at different initial current setpoints (different tip–sample separations). In the absence of TIBB there will be negligible change in the band edges of the spectra; however, if the spectra are strongly influenced by TIBB, increasing the current setpoint (reducing tip–sample separation) will lead to increased band bending, and overestimation of the bandgap[37]. As shown in Fig. 4b the exact opposite is observed for few-layer Na_3Bi. In this case the bandgap becomes smaller, closes and then re-opens upon increasing the current (and consequently electric field), and is clearly not consistent with TIBB. However, we also cannot rule out whether the dI/dV spectra taken at low currents (low fields) (as shown in Fig. 2) are intrinsic or free from TIBB.

In order to estimate the effects of TIBB, we first adopt a model based on a uniformly charged sphere[37], with the analytic expression for the difference ϕ_{BB} between the apparent (measured) and actual energy position of a spectral feature (for example, band edge) due to TIBB being given by:

$$\phi_{BB}(V_b, r, h, \varepsilon) = \frac{1}{1+\varepsilon\frac{h}{r}}(eV_b - W_0) \quad (3)$$

where ε is the dielectric constant, V_b is the bias voltage, h the tip height, r the tip radius and W_0 the work function difference between sample and tip (that is, $W_0 = W_{sample} - W_{tip}$). We use $h = 1.5$ nm and $W_0 = -1.2$ eV (taken from calculations in Methods section 'Calculating tip–sample separation and electric field') and assume a tip radius $r = 25$ nm. For the static dielectric constant, we use the value[14] for bulk Na_3Bi, $\varepsilon = 120$. While the dielectric constant in ML and BL Na_3Bi could be very different, the bulk value is currently the only available value and is used as a rough estimate. Extended Data Fig. 3d plots ϕ_{BB} as a function of bias voltage calculated from equation (3). The correction factor for TIBB is given by $1 / \left(1 - \frac{\partial\phi}{\partial V}\right)$, which yields 1.13 for Na_3Bi.

The uniformly charged sphere model is known to overestimate TIBB by almost a factor of 2 when more detailed modelling that incorporates charge redistribution is taken into account[37]. Therefore, we adopt the image charges method for a charged sphere in front of a dielectric sample (see Appendix from ref. [37]). In this case the TIBB expression is replaced by:

$$\phi_{BB}(V_b, r, h, \varepsilon) = F(r, h, \varepsilon)(eV_b - W_0) \quad (4)$$

where F is the ratio of the electrical potential on the tip surface and at the point of the sample closest to the tip. For $h = 1.5$ nm, $r = 25$ nm and $\varepsilon = 120$ we find that $F = 0.064$, yielding a TIBB correction factor of 1.07, meaning our best estimate is that the measured bandgap of ultrathin Na_3Bi includes a systematic overestimation due to TIBB of 7%. For ML and BL Na_3Bi with bandgaps of 360 meV and 300 meV this corresponds to 25 meV and 21 meV respectively. Because this is comparable to the random error of ±25 meV as discussed in Methods section 'Bandgap extraction from STM spectra', we have not corrected for TIBB.

DFT calculations for Na(2) vacancy Na_3Bi layers and Z2 calculations. The calculated band structures of Na_3Bi ML and BL with an Na(2) vacancy including spin–orbit coupling (SOC) are displayed in Extended Data Fig. 4b and g, respectively. Bandgaps of 0.30 eV (0.28 eV) and 0.22 eV (0.16 eV) are obtained for ML (without structural relaxation) and BL respectively, with the bandgaps obtained from DFT using the Quantum Espresso code and the value obtained from the VASP package in brackets. The non-trivial topological character can be intuitively observed from the orbital components of the band edge states. Without SOC (as shown for ML and BL in Extended Data Fig. 4c and h respectively), the conduction band minimum (CBM) is mainly contributed by Na s and Bi s orbitals, whereas the valence band maximum (VBM) is mainly from the Bi p_x/p_y orbitals, showing a normal band ordering. After including SOC (shown in Extended Data Fig. 4d and i for ML and BL respectively), the band ordering is inverted at Γ, with p orbitals at the CBM above the s orbitals at the VBM. This SOC-induced band inversion marks a topologically non-trivial phase, which indicates that both ML and BL Na_3Bi are nontrivial 2D topological insulators. The edge state spectrum is shown in Extended Data Fig. 4e for ML and in Extended Data Fig. 4j for BL. The projected 1D Brillouin zone is shown in Extended Data Fig. 4a. One can clearly observe a Kramers pair of topological edge states. To prove these systems are non-trivial, we determine the topological invariant of both systems. This is done by employing the Wilson loop method[38,39], in which one traces the evolution of the Wannier function centres, as plotted in Extended Data Fig. 1f and k. From the calculation, we confirm that both ML and the BL Na_3Bi with and without Na(2) vacancies are topologically non-trivial with the invariant $\mathbb{Z}_2 = 1$.

Extracting and fitting the ARPES band dispersion of few-layer Na_3Bi. Energy dispersion curves (EDCs) and momentum dispersion curves (MDCs) are slices through constant momentum and constant energy of the photoemission spectra (such as Extended Data Fig. 5a) along high-symmetry directions (M–Γ–M) or (K–Γ–K). Band energy and momentum coordinates are extracted by Gaussian fitting of the photoemission intensity on a flat background (as shown in Extended Data Fig. 5b, c by the blue circles). We find that band edges are extracted more reliably from EDCs, while MDC peak positions are used at larger binding energies where clearly distinct peaks can be resolved (see left panel of Extended Data Fig. 5b).

The measured bands are observed to fit hyperbolae as shown in Extended Data Fig. 5d, as expected of gapped Dirac systems. Fits of the bands to a parabola are much poorer, as shown in Extended Data Fig. 5e. In order to accurately model the band dispersion of a 2D gapped Dirac system, we use a bi-partite model for the valence (p) and conduction (n) bands that assumes the form:

$$(E_{B,i} - D)^2 = \Delta_i^2 + \hbar^2 v_{F,i}^2 (k + k_0)^2, i \in p, n \quad (5)$$

where $\Delta = \Delta_n + \Delta_p$ represents the energy gap, v_{Fi} the asymptotic Fermi velocities at large momenta, E_B the binding energy, and D a doping or energy-shift of the bands.

The velocities v_{Fi} measured for the valence and conduction bands for both films are nearly independent of K dosing, with near-isotropic dispersion in k_x, k_y (also shown in Extended Data Fig. 6). Hence we take v_{Fn} and v_{Fp} to be a global fit parameter, with best fit values $v_{Fn} \approx 1 \times 10^6$ m s^{-1} and $v_{Fp} \approx 3 \times 10^5$ m s^{-1}.

We then fit the valence band photoemission—that is, the negative solution for equation (5)—using the global v_{Fp} parameter, allowing us to determine Δ_p and D as a function of K dosing. A monotonic increase of D with K dosing is observed as expected, reflecting the shift of the valence band to larger binding energy.

The photoemission intensity of the electron band is two orders of magnitude less than that of the valence band—possibly due to the different orbital characters of the two bands resulting in a lower intensity due to matrix element effects. Owing to the large bandgap of few-layer Na_3Bi, the conduction band lies well above the Fermi level in the as-grown film, meaning that significant charge transfer from K dosing is needed to n-type dope the film in order to observe the conduction band. As such the fitting parameter Δ_n for the electron bands can only be determined once the conduction band is resolvable below E_F, and in addition further seen to match the valence band determined value for D. Values for $\Delta_{n,p}$ as a function of electric displacement field are addressed in Methods section 'Electric displacement field dependence from ARPES'.

Mapping from K deposition to electric displacement field. Potassium deposited on the Na_3Bi surface donates electrons leaving a positive K^+ ion behind, producing a uniform planar charge density. This is equivalent to a parallel plate capacitor, allowing the electric displacement field, D, to be calculated across the Na_3Bi film using Gauss' law via:

$$D = \frac{E}{\varepsilon} = \frac{eQ}{\varepsilon_0} = \frac{e\Delta n}{\varepsilon_0} \quad (6)$$

with Q representing the total charge transferred due to potassium doping, that is, $Q = \Delta n$. The charge transfer to the system cannot be directly inferred when a Fermi surface cannot be clearly resolved, so our calculations make use of the conduction band Fermi surface that becomes distinct after 15 min of K dosing. As seen in Extended Data Fig. 6a, the n-type Fermi surface is a nearly isotropic Dirac cone. By measuring k_F as a function of K dosing either from EDCs or a Fermi surface map as in Extended Data Fig. 6b, the charge density can be directly calculated using:

$$n(k_F) = \frac{g}{4\pi} k_F^2 \quad (7)$$

where a band degeneracy of $g = 4$ can be taken for Dirac systems[14]. The charge density $n(k_F)$ is also consistent with the assumption of a Dirac dispersion centred at D, that is, $k_F = D/\hbar v_F$.

The change in $n(k_F)$ as a function of K dosing is approximately 2×10^{12} cm^{-2} between consecutive K dosing until the 50-min mark (where charge saturation occurs). By assuming that in this regime every K atom donates one electron and a constant dose rate we can extrapolate the total $n(k_F)$ back to the doping of the as-grown film growth. For the as-grown film this corresponds to a p-type doping of 4×10^{12} cm^{-2}. From this as-grown doping we can then calculate the electric displacement field using equation (6), as shown on the right hand axis of Extended Data Fig. 6c.

Electric displacement field dependence from ARPES. Next we map the calculated $\Delta_{n,p}$ (which reflects the size of the bandgap) at different K dosing to a corresponding electric displacement field, as shown in Extended Data Fig. 7a. The purple circles in Extended Data Fig. 7a represent where $\Delta_{n,p}$ are directly extracted

from the bi-partite model of the experimental data. At low displacement field, where the conduction band is still above the Fermi level, we cannot directly obtain a value for Δ_n. We estimate the size of Δ_n at these low displacement fields using the ratio $(\Delta_p + \Delta_n)/\Delta_p \approx 1.4$, which is directly obtained from the purple points. For the as-grown sample this yields a value of ~320 meV, which, given we cannot directly measure the conduction band edge, is in reasonable agreement with the experimental result from STS, and the theoretical DFT value. The reduction in bandgap is consistent with the independently measured gap-closing from STS in Fig. 4c, with the relative energy separation of the electron and valence bands narrowing monotonically with increasing field. When the estimated bandgap $\Delta = \Delta_n + \Delta_p$ becomes as small as 100 meV (corresponding to displacement fields >1.5 V nm^{-1}), it is comparable to the intrinsic energy broadening of the bands (particularly the valence band). Therefore, we cannot definitely conclude from ARPES measurements whether the bandgap completely closes after this point or is re-opened again.

Calculating tip–sample separation and electric field. In STM for a simple square barrier the tunnelling current (in atomic units) follows:

$$I_t = I_0 e^{-2(z-z_0)\cdot\sqrt{2\Phi}} \tag{8}$$

where Φ is the work function of the energy barrier and z and z_0 the tip and sample positions, respectively, such that the distance between tip and sample is $s = z - z_0$. This allows the work function of the barrier to be obtained by measuring the tunnelling current as a function of tip position, then extracting the slope of $\ln(I_t)/z$:

$$\frac{\mathrm{d}\ln(I)}{\mathrm{d}z} = -2\sqrt{2\Phi} \tag{9}$$

Extended Data Fig. 8 shows logarithmic plots of the tunnelling current as a function of relative distance for Au(111) (bias 500 mV) (Extended Data Fig. 8a) and thin-film Na_3Bi (bias −300 mV) where the absolute current is plotted (Extended Data Fig. 8b). For Au(111) the characteristic exponential dependence of $I(z)$ (straight line on the semi-log plot) is observed with current increasing from 0.01 nA to 10 nA by moving the tip 3 Å closer to the surface. However, it is immediately clear that very different behaviour occurs for Na_3Bi in Extended Data Fig. 8b. At low tunnelling current an exponential dependence with distance $I(z)$ is observed, but as the distance from tip and sample decreases the current saturates to a value around 1 nA, which occurs over a length scale of ~1 nm. This corresponds to the barrier height going to zero as the tip approaches the sample surface.

This effect results from a modification of equation (8) due to the lowering of the potential barrier by the mirror potential seen by an electron in close proximity to a metal surface[40], and is most pronounced for low-work-function materials, such as Na_3Bi. This is shown schematically in Extended Data Fig. 8c. As we show in detail below, the theoretical treatment indicates that the effect of the mirror potential at large distances is simply a rigid shift in distance of the region in which the exponential behaviour occurs. Thus, we can use the exponential region where equation (8) is obeyed to determine the work function, and we can extrapolate equation (8) to point contact to determine the tip–sample distance, provided a correction factor is applied to account for the rigid shift due to the mirror potential.

There has been significant work on modelling image potential effects, well summarized in ref. [41], whereby considering a simple model such as the square barrier depicted in Extended Data Fig. 8c for long tip–sample distances, $\ln(2)/s \gg \Phi$, the tunnelling current can be expressed as:

$$I_t = I_0 e^{-2z\cdot\sqrt{2\Phi}} e^{\ln(2)\cdot\sqrt{2/\Phi}} \tag{10}$$

where the main effect of the image potential at very long tip–sample distances is to increase the tunnelling current by a constant factor $e^{\ln(2)\cdot\sqrt{2/\Phi}}$. For $I_t = I_0$, we obtain the increased distance between tip and sample due to the image potential $s = \ln(2)/2\Phi$ in atomic units. Converting from atomic units to SI units gives

$$\begin{aligned} s(\text{Å}) &= \left(\frac{\ln(2)}{2\Phi(\text{eV})}\right) \times 1\ \text{Bohr(Å)} \times 1\ \text{Hartree(eV)} \\ &= \left(\frac{\ln(2)}{2\Phi(\text{eV})}\right) \times 0.529\ \text{Å} \times 27.2\ \text{eV} \end{aligned}$$

such that equation (8) would underestimate z_0 by a distance of 5 Å/[Φ(eV)].

This value, however, is most probably an underestimate, as shown in Extended Data Fig. 8d (taken directly from figure 10 of ref. [41]) where $\ln(I(s)/I_0)$ as a function of distance is plotted for the simple square barrier model described above (dashed line), and more sophisticated calculations incorporating DFT-LDA (full line) and a model developed by Pitarke et al., that accounts for both non-local and local exchange and correlation effects (dashed-dotted red line)[42]. At large s the models still show an exponential $I(s)$ with similar slope (Extended Data Fig. 8d) but the distance at which similar current is achieved is increased by as much as a factor of 3 from the square barrier model, such that the underestimation of z_0 distance by equation (8) is more likely to be ~15 Å/[Φ(eV)][42].

To understand and quantify the tip–sample distance in Na_3Bi, we first extract the slope from the linear region in Extended Data Fig. 8b (as shown by the black line). This fit yields a slope of 1.5 Å^{-1}, and accounting for the bias of −300 mV yields a work function or barrier height of 2.3 eV. I versus z measurements (where z is the nominal distance between tip and sample as defined by the STM piezo controller with arbitrary zero) were taken at various negative and positive bias values and yielded work functions of 2.3 ± 0.05 eV. This confirms a very low barrier height. From the above analysis, we estimate that the effect of the mirror potential is to lead to an underestimation of z_0 in equation (8) of ~15 Å/2.3 or ~6.5 Å.

In order to determine the exact value of z_0, we assume that at $z_0 = 0$ (point contact) the conductance is of the order of the conductance quantum $e^2/h \approx 40\ \mu$S, which gives $I_0 = 12\ \mu$A at a bias voltage of −300 mV. Then the fit to the exponential region of $I(z)$ in Extended Data Fig. 8b to equation (10) gives $z_0 = -13.2$ Å. This allows us to plot the absolute distance $s = z - z_0$ on the top axis of Extended Data Fig. 8b.

We are now in a position to estimate the tip–sample separation from the dI/dV measurements. For each dI/dV curve we extract a relative distance s for each dI/dV measurement by referencing the tunnelling current at −300 mV to the I versus s data in Extended Data Fig. 8b.

The green and purple dI/dV spectra in Fig. 4b are treated in the following manner:

Green curve. At a bias of −300 mV this has a tunnelling current of 26 pA. From the I versus z plot taken at −300 mV this corresponds to relative z distance of 1.3 Å. Adding 13.2 Å to account for point contact and mirror potential yields a tip–sample separation of 14.5 Å.

Purple curve. At a bias of −300 mV this has a tunnelling current of 570 pA. From the I versus z plot taken at −300 mV this corresponds to a relative z distance of −3 Å. Adding 13.2 Å to account for point contact and mirror potential yields a tip–sample separation of 10.2 Å.

We now have an estimate of the tip–sample separation, so to calculate a displacement field for each of our dI/dV measurements we need to calculate the potential difference, that is, the work function difference between the metallic tip and the few-layer Na_3Bi. The measured barrier height of 2.3 eV is an average of the tip and sample work functions, $\Phi_{\text{Barrier}} = (\Phi_{\text{Tip}} + \Phi_{\text{Na3Bi}})/2$, meaning we need to know either the tip work function or measure the work function of the Na_3Bi.

The Kelvin probe technique was used to measure the work function of few-layer Na_3Bi. The work function was determined by measuring the contact potential difference of the Na_3Bi relative to a gold reference of known work function (determined by photoelectron spectroscopy secondary electron cutoff measurements). A work function for few-layer Na_3Bi of 1.7 ± 0.05 eV was measured using this technique. This value and the 2.3 eV potential barrier gives a tip work function of 2.9 ± 0.05 eV, and a potential difference between tip and sample of 1.2 ± 0.1 eV. It should be noted that this is significantly lower than the expected value for a PtIr tip, suggesting that Na atoms have been picked up by the tip and consequently lower the work function (work function of Na is 2.23 eV). While Na atoms were picked up they have little influence on the tip density of states, as spectroscopy performed on Au(111) after measurements on Na_3Bi were completed revealed a flat LDOS near the Fermi energy.

Using the calculated potential difference and tip–sample separation from above allows us to calculate electric fields for dI/dV spectra on ML and BL Na_3Bi, as shown in Fig. 4b for BL and in Extended Data Fig. 9 for ML, with the full data set of bandgap as a function of electric field shown in Fig. 4c.

The above discussion reflects our best estimate of the electric field magnitude. However, we estimate that the electric field could be incorrect by as much as 50% due to the main source of error in estimating the correction for the mirror potential. An estimate of this can be made by comparing the correction we employed and the correction based on the square barrier model which is 3 times smaller. This ~4 Å smaller correction would lead to a large increase in electric field, ~50%. In addition, there are small sources of error that arise from the error in the Na_3Bi work function and in the fit of the slope of d$\ln(I)$/dz, the potential difference and barrier height. However, these errors are expected to be no more than 10%. Regardless, the qualitative behaviour—that is, closing and re-opening of the bandgap with increasing electric field—is correct and independent of knowing the exact electric field magnitude.

DFT calculations of electric-field-induced topological phase transition. In order to confirm our predicted experimental observation of a topological phase transition, DFT calculations were performed on ML Na_3Bi with an Na(2) surface vacancy as a function of electric field, as shown in Extended Data Fig. 10. Extended Data Fig. 10a plots the bandgap variation as a function of electric field for ML Na_3Bi with an Na(2) vacancy. The critical field where the bandgap closes and

then reopens is 1.85 V Å^{-1}. This value is an order of magnitude larger than the experimental result of ~1.1 V nm^{-1}. A possible explanation is that in the modelling there is 1 Na vacancy per 2 × 2 supercell (an order of magnitude greater than the defect density observed experimentally). These charged defects would be expected to induce stronger screening of external electric fields, which tends to make the critical electric field overestimated compared to experiment.

Importantly, the DFT results clearly demonstrate the topological phase transition, as shown in Extended Data Fig. 10c–f. In Extended Data Fig. 10c, at 0 V Å^{-1}, the orbital resolved band structure clearly shows a band inversion of the *s* and *p* atomic orbitals at Γ induced by SOC. This clearly indicates a non-trivial 2D topological insulator, as shown in the corresponding projected edge spectrum in Extended Data Fig. 10d with the observation of topological edge states. In Extended Data Fig. 10e, the orbital resolved band structure above the critical field value where the gap has reopened has undergone a band ordering change at Γ as compared with Extended Data Fig. 10c. This indicates a topological to trivial insulator phase transition with electric field, and is confirmed by the disappearance of the topological edge states in Extended Data Fig. 10f.

Summary of crystalline symmetries for ML and BL Na_3Bi. The preservation and breaking of discrete symmetries under the effects of an out-of-plane *E*-field, as well as the presence of an Na(2) vacancy, are tabulated in Extended Data Fig. 11a and b for ML and BL Na_3Bi, respectively.

Notes on nomenclature. (1) C_{nx} and C_{nz} are rotations of 360°/*n* with the rotation axis along the *x* direction and the *z* direction, respectively. (2) S_{nz} is a rotation of 360°/*n* followed by reflection in a plane perpendicular to the rotation axis (along the *z* direction). (3) M_{xy}, M_{xz} and M_{yz} are mirror reflections with the mirror in the *x*–*y* plane, the *x*–*z* plane and the *y*–*z* plane, respectively. (4) *I* is inversion symmetry. (5) Symmetry relations: $S_{3z} = C_{3z}M_{xy}$; $M_{xz} = C_{2x}M_{xy}$; $S_{6z} = IC_{3z}$; $M_{yz} = IC_{2x}$.

Na_3Bi monolayer (ML). For ML without an Na(2) vacancy, the space group is $P\bar{6}m2$ (no. 187). The point group is D_{3h}. Both electric field and Na(2) vacancy break the horizontal mirror symmetry, details are summarized in Extended Data Fig. 11a. Extended Data Fig. 11 shows the Na_3Bi crystal structure for pristine ML (Extended Data Fig. 11c), with an Na surface vacancy (Extended Data Fig. 11d) and with an Na surface vacancy and electric field (Extended Data Fig. 11e).

Na_3Bi bilayer (BL). For BL without an Na(2) vacancy, the space group is $P\bar{3}m1$ (no. 164). The point group is D_{3d}. Both electric field and Na(2) vacancy break the inversion symmetry, details are summarized in Extended Data Fig. 11b. Extended Data Fig. 11 shows the Na_3Bi crystal structure for pristine BL (Extended Data Fig. 11f), BL with an Na surface vacancy (Extended Data Fig. 11g) and BL with an Na surface vacancy and electric field (Extended Data Fig. 11h).

One can observe that both BL and ML Na_3Bi possess C_{3z} and C_{2x} rotational symmetries. The difference is that ML has mirror symmetry M_{xy} and BL has inversion symmetry *I*. In terms of symmetry breaking, the electric field does not break any additional symmetry that is not already broken by the Na(2) vacancy. For ML, both electric field and Na(2) vacancy break the horizontal mirror symmetry and C_{2x} rotation symmetry, and reduce the D_{3h} symmetry to C_{3v} symmetry; while for BL, they both break the inversion symmetry and C_{2x} rotation symmetry, and reduce the D_{3d} symmetry to C_{3v} symmetry. Hence, ML and BL share the same point group C_{3v} after symmetry breaking by electric field or Na(2) vacancy.

However, for our discussion on the band topology, the crystalline symmetry is not relevant. This is because our main point is that in the absence of electric field, the ML/BL Na_3Bi (with or without Na vacancies) are QSH insulators, which only require time reversal symmetry. Electric field does not break the time reversal symmetry, rather it drives a QSH insulator $\upsilon \in \mathbb{Z}_2 = 1$ to trivial insulator $\upsilon \in \mathbb{Z}_2 = 0$ transition through a band ordering inversion due to the Stark effect.

Data availability

The data that support the findings of this study are available from the corresponding author upon reasonable request.

26. Blöchl, P. E. Projector augmented-wave method. *Phys. Rev. B* **50**, 17953–17979 (1994).
27. Perdew, J. P., Burke, K. & Ernzerhof, M. Generalized gradient approximation made simple. *Phys. Rev. Lett.* **77**, 3865–3868 (1996).
28. Souza, I., Marzari, N. & Vanderbilt, D. Maximally localized Wannier functions for entangled energy bands. *Phys. Rev. B* **65**, 035109 (2001).
29. Lopez Sancho, M. P., Lopez Sancho, J. M., Sancho, J. M. L. & Rubio, J. Highly convergent schemes for the calculation of bulk and surface Green functions. *J. Phys. F* **15**, 851–858 (1985).
30. Wu, Q., Zhang, S., Song, H. F., Troyer, M. & Soluyanov, A. A. WannierTools: An open-source software package for novel topological materials. *Comput. Phys. Commun.* **224**, 405–416 (2018).
31. Becke, A. D. & Johnson, E. R. A simple effective potential for exchange. *J. Chem. Phys.* **124**, 221101 (2006).
32. Tran, F. & Blaha, P. Accurate band gaps of semiconductors and insulators with a semilocal exchange-correlation potential. *Phys. Rev. Lett.* **102**, 226401 (2009).
33. Koller, D., Tran, F. & Blaha, P. Improving the modified Becke-Johnson exchange potential. *Phys. Rev. B* **85**, 155109 (2012).
34. Edmonds, M. T., Hellerstedt, J., O'Donnell, K. M., Tadich, A. & Fuhrer, M. S. Molecular doping the topological Dirac semimetal Na_3Bi across the charge neutrality point with F4-TCNQ. *ACS Appl. Mater. Interfaces* **8**, 16412–16418 (2016).
35. Damascelli, A., Hussain, Z. & Shen, Z.-X. Angle-resolved photoemission studies of the cuprate superconductors. *Rev. Mod. Phys.* **75**, 473–541 (2003).
36. Hufner, S. *Photoelectron Spectroscopy: Principles and Applications* 3rd edn (Springer, Berlin, 2003)
37. Battisti, I. et al. Poor electronic screening in lightly doped Mott insulators observed with scanning tunneling microscopy. *Phys. Rev. B* **95**, 235141 (2017).
38. Yu, R., Qi, X. L., Bernevig, A., Fang, Z. & Dai, X. Equivalent expression of Z2 topological invariant for band insulators using the non-abelian Berry connection. *Phys. Rev. B* **84**, 075119 (2011).
39. Soluyanov, A. A. & Vanderbilt, D. Wannier representation of Z2 topological insulators. *Phys. Rev. B* **83**, 035108 (2011).
40. Lang, N. D. Apparent barrier height in scanning tunnelling microscopy. *Phys. Rev. B* **37**, 10395–10398 (1988).
41. Blanco, J. M., Flores, F. & Perez, R. STM-theory: image potential, chemistry and surface relaxation. *Prog. Surf. Sci.* **81**, 403–443 (2006).
42. Pitarke, J. M., Echenique, P. M. & Flores, F. Apparent barrier height for tunneling electrons in STM. *Surf. Sci.* **217**, 267–275 (1989).

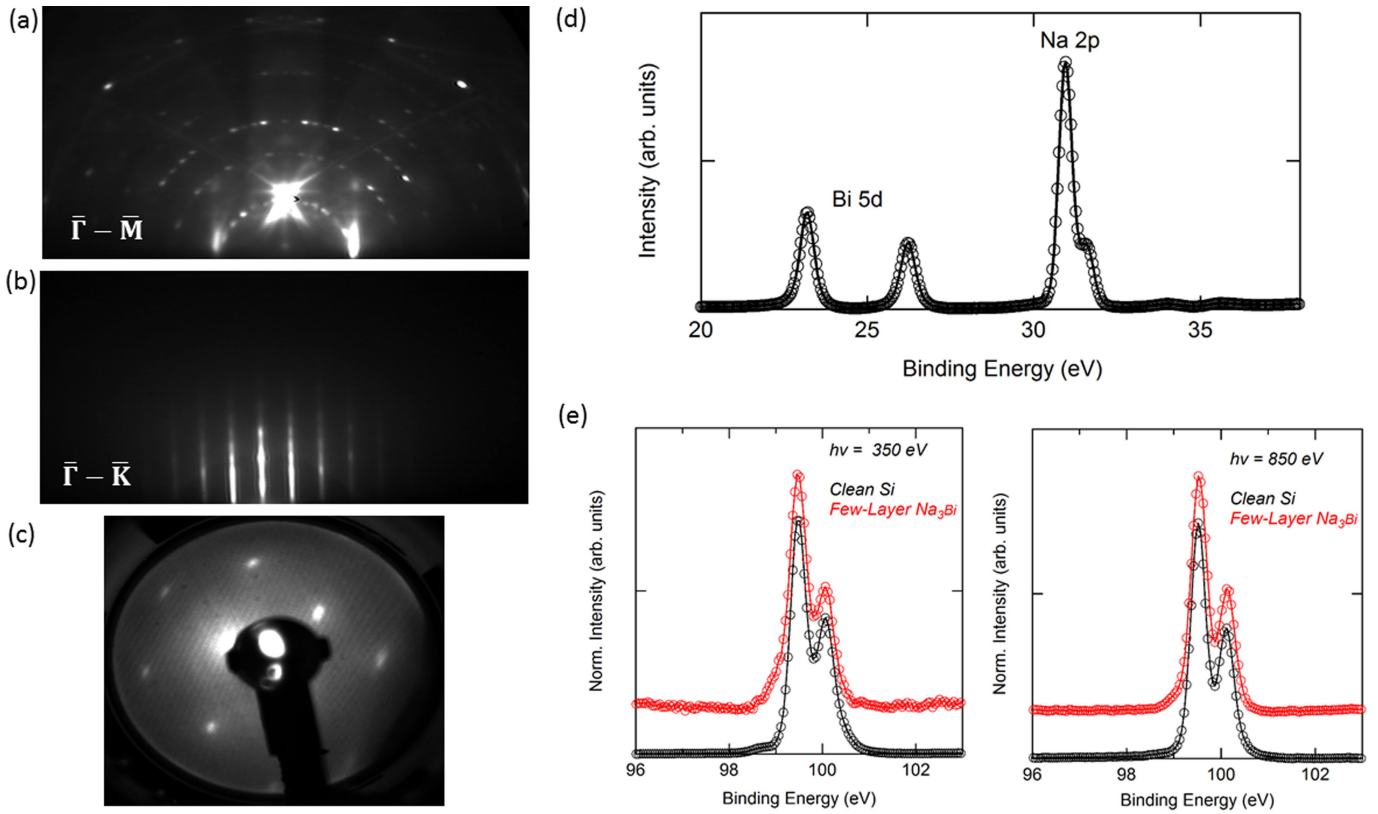

Extended Data Fig. 1 | RHEED, LEED and XPS characterization of few-layer Na_3Bi. a, **b**, RHEED patterns of Si(111) 7 × 7 reconstruction along the $\bar{\Gamma}-\bar{M}$ direction (**a**) and of few-layer Na_3Bi along the $\bar{\Gamma}-\bar{K}$ direction (**b**). **c**, 1 × 1 LEED image of few-layer Na_3Bi taken at 32 eV. **d**, XPS of Na 2*p* and Bi 5*d* core level taken at $hv = 100$ eV for few-layer Na_3Bi. **e**, Normalized XPS of Si 2*p* core level taken at 350 eV (left panel) and at 850 eV (right panel). Each panel shows the Si 2*p* of the clean Si substrate (black curve) and with few-layer Na_3Bi grown on top (red curve). The spectra have been offset in intensity for clarity.

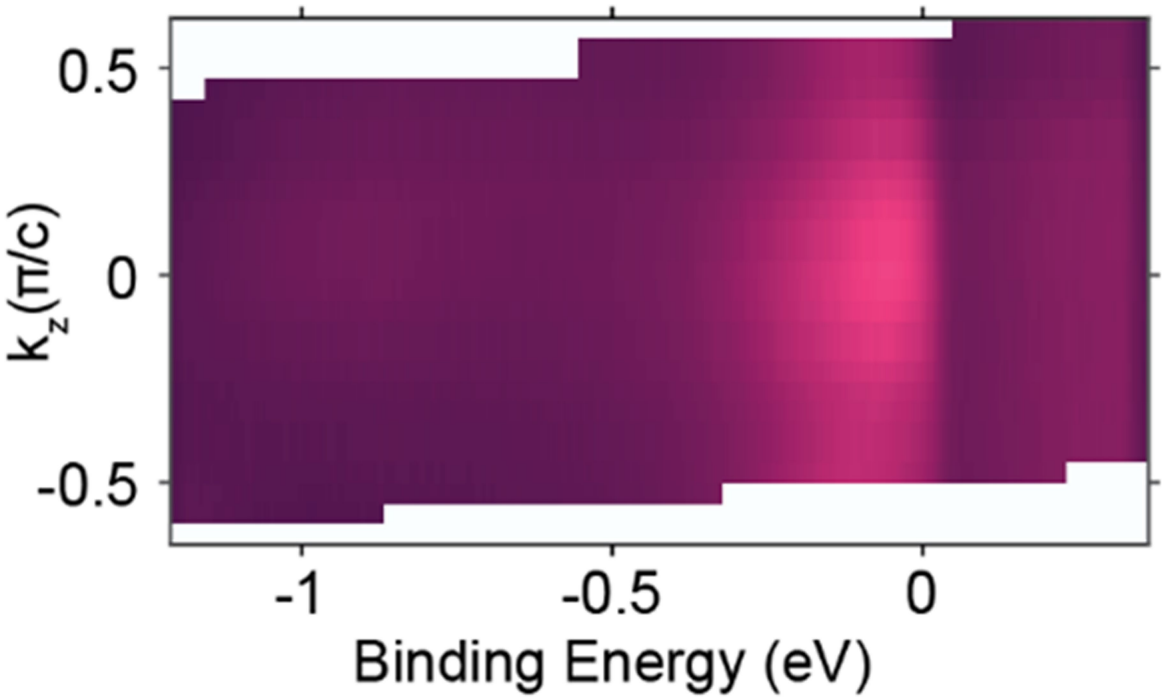

Extended Data Fig. 2 | k_z band dispersion of few-layer Na_3Bi from photon-energy-dependent ARPES measurements. These photon-energy-dependent ARPES measurements of ML/BL Na_3Bi demonstrate effectively 2D dispersion. The figure shows a cut through the photon-energy-dependent ($h\nu = 45$–55 eV) Fermi surface, demonstrating non-dispersion of the gapped Dirac valence band along k_z, with the intensity of emitted photoelectrons reflected in the colour scale.

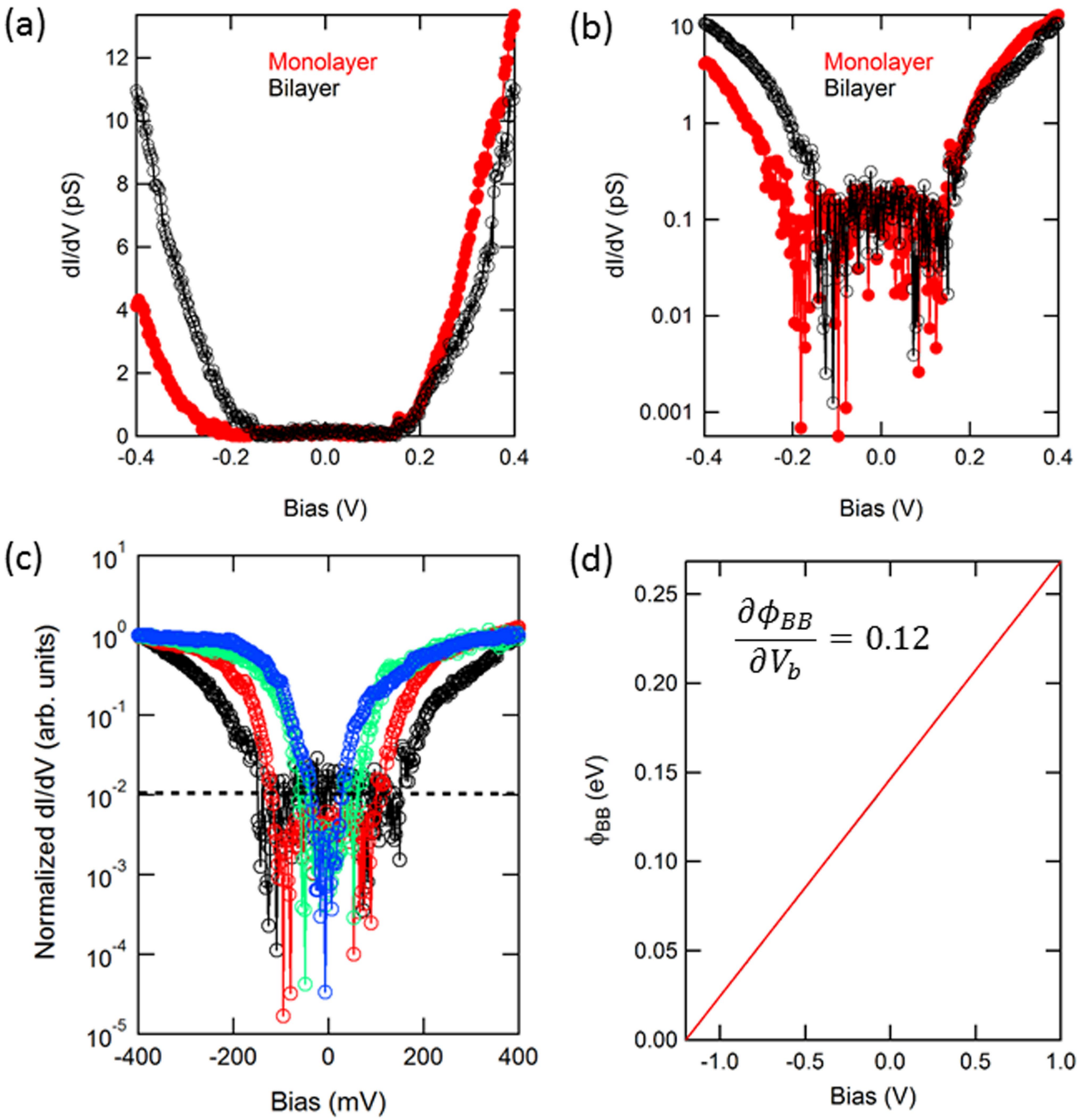

Extended Data Fig. 3 | Bandgap extraction from scanning tunnelling spectra. a, **b**, dI/dV spectra taken for ML (red) and BL (black) Na_3Bi plotted on a linear (**a**) and a logarithmic (**b**) scale. The logarithmic scale better accounts for the large change in intensity near the band edge. **c**, Normalized dI/dV spectra at various tip–sample separations, illustrating that the onset in intensity typically occurs at a normalized dI/dV signal of 0.01 within an error of ±25 meV (when also accounting for tip-induced band bending). **d**, Calculated tip-induced band bending, ϕ_{BB}, using equation (3) for different biases.

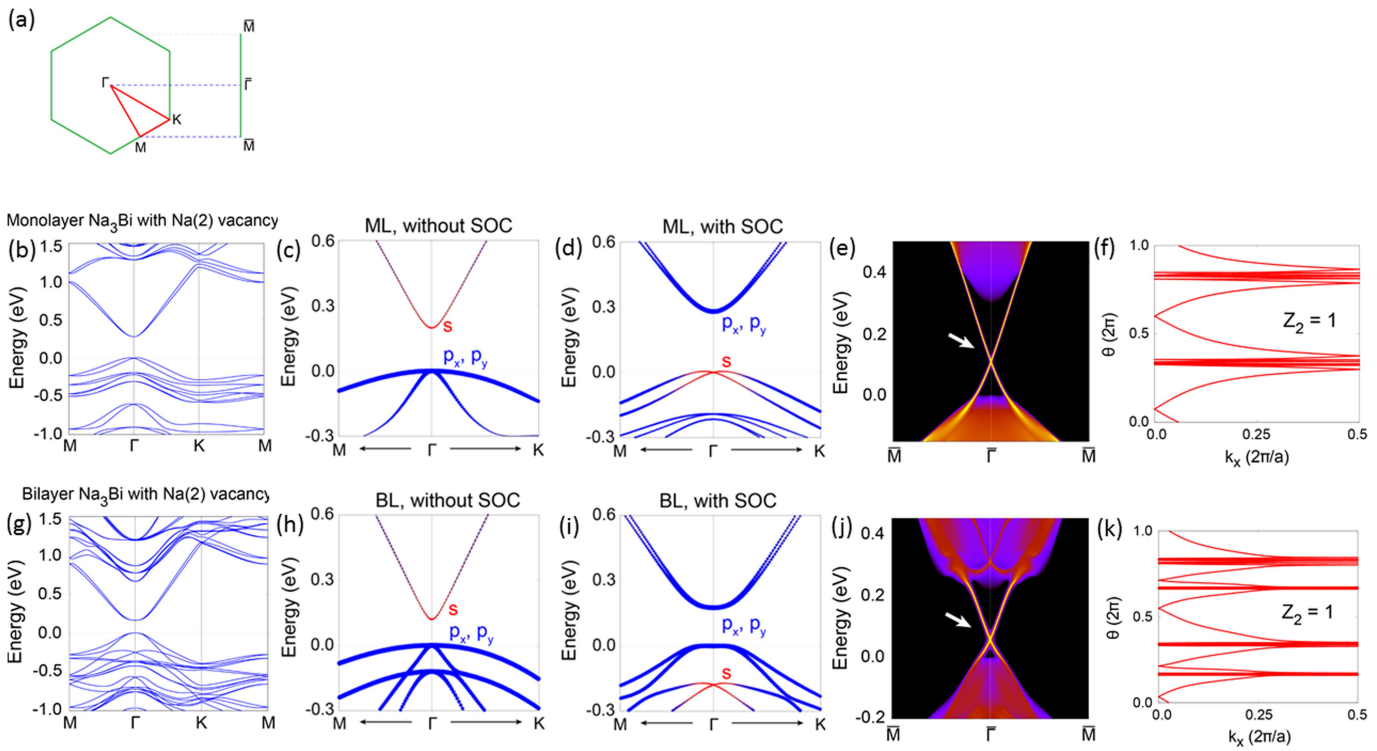

Extended Data Fig. 4 | DFT calculations on the topological nature of Na_3Bi layers. a, 2D Brillouin zone for Na_3Bi layered structures. Here we also show the projected 1D Brillouin zone used for studying the edge spectrum. **b**–**h**, Results for ML (**b**–**f**) and BL (**g**–**k**) Na_3Bi with Na(2) vacancies (with one Na(2) vacancy in a 2×2 supercell). **b**, **g**, Electronic band structures, where the energy zero is set to be at the valence band maximum. **c**, **h**, Orbitally resolved band structure without SOC and **d**, **i**, orbitally resolved band structure with SOC. The red dots represent the contribution from the Na *s* and Bi *s* atomic orbitals, and the blue dots represent contribution from the Bi p_x/p_y atomic orbitals. Band inversion induced by SOC can be clearly observed at the Γ point for both ML and BL cases, which indicates that both ML and BL Na_3Bi are non-trivial 2D topological insulators. **e**, **j**, Projected edge spectrum (edge along the [010] direction), where pairs of $\mathbb{Z}_2$ topological edge states can be observed in the energy gaps (marked by the white arrows) where the colour scale reflects the spectral weight. **f**, **k**, Calculated Wannier function centre evolutions, which indicate a nontrivial $\mathbb{Z}_2$ invariant ($\mathbb{Z}_2 = 1$) for the bulk band structure in both ML and BL.

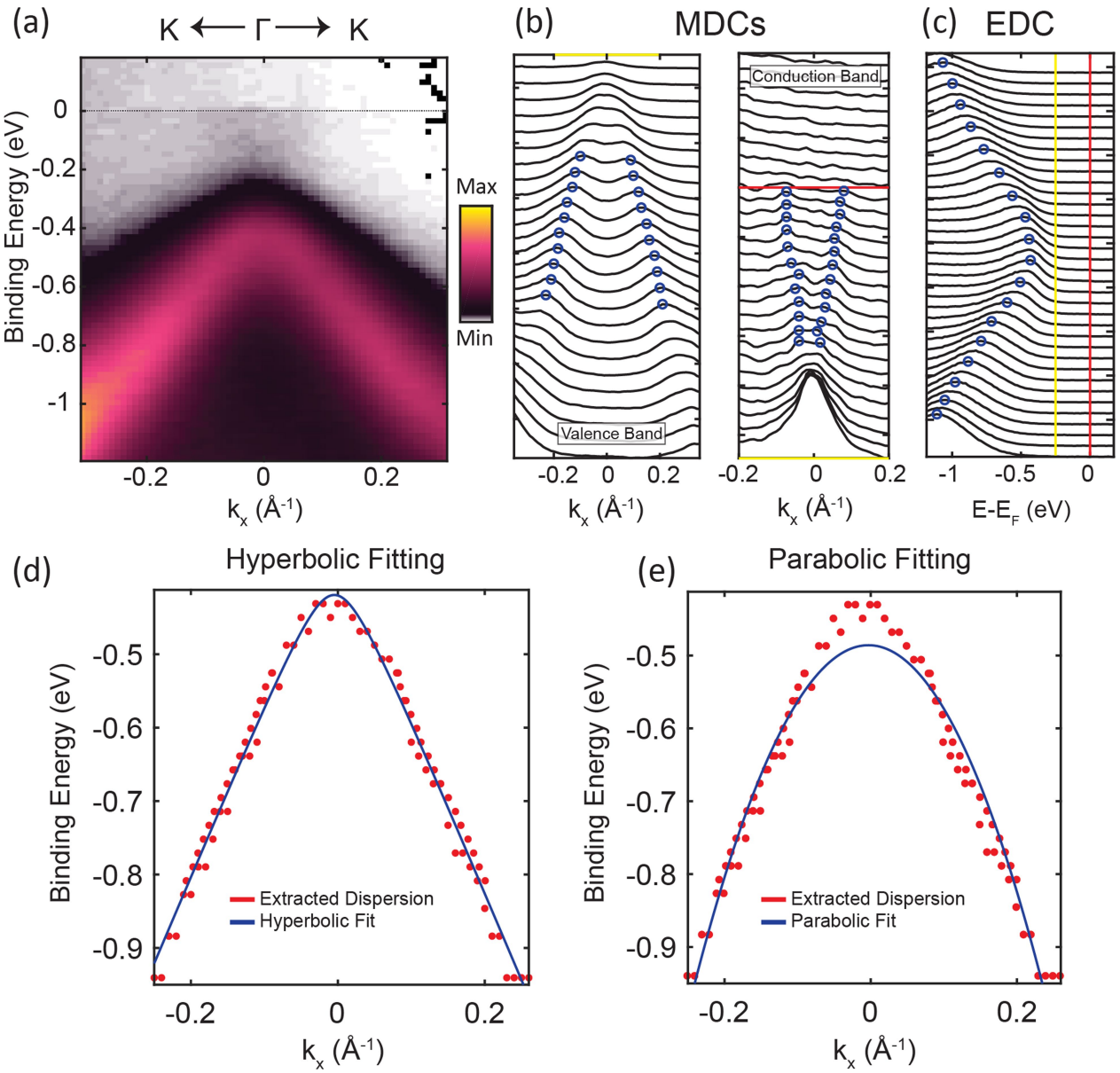

Extended Data Fig. 5 | Extracting and fitting the dispersion relation from ARPES MDC and EDC spectra of few-layer Na_3Bi. a, ARPES intensity plot (colour scale at right) along the K–Γ–K direction after 30 min of K dosing. **b**, Stack plots of MDCs for the valence band (left panel) and conduction band (right panel) extracted from **a**, where the blue circles represent the Gaussian-fit band locations. Red and yellow lines mark shared constant-energy k_x vertices used throughout **b** and **c**. **c**, EDCs extracted from **a**. **d**, **e**, Fitting band coordinates that have been extracted by MDC and EDC analysis (red dots) to a hyperbola (**d**) and to a parabola (**e**), showing that Na_3Bi-like bands are best described by a hyperbola function.

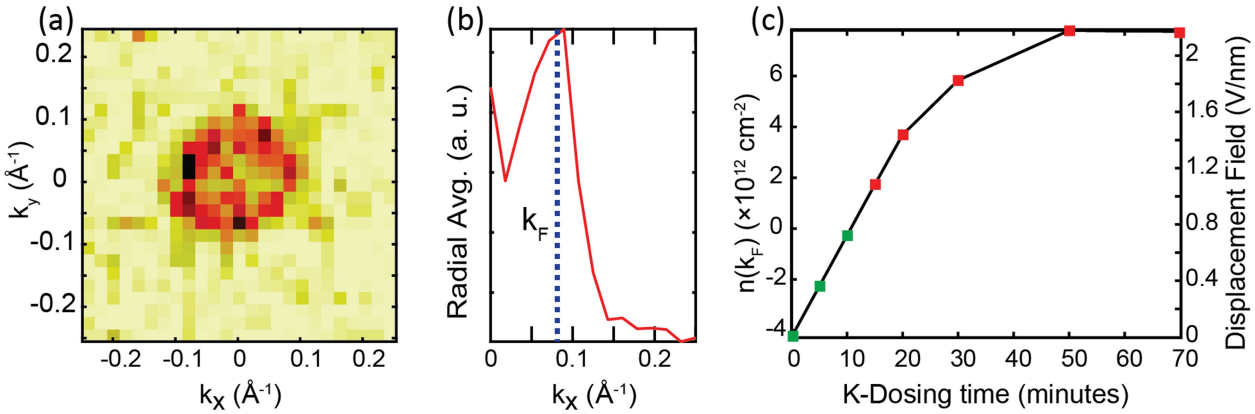

Extended Data Fig. 6 | Displacement field calculations from K dosing in ARPES. a, Electron-band Fermi surface of few-layer Na_3Bi after 30 min of K dosing, where the colour scale reflects the intensity of emitted photoelectrons at the Fermi energy. **b**, Red line, radially averaged momentum profile through the Fermi surface, showing the ring structure at k_F (dashed blue line shows position of k_F). **c**, Calculated charge density (left-hand *y* axis) using equation (7) and the corresponding electric displacement field (right-hand *y* axis) associated with the net charge transfer from the as-grown film as a function of K-dosing time. Red points are as-measured, and green points are extrapolated based on the E_F shifting rate with K dosing between 15 min and 50 min.

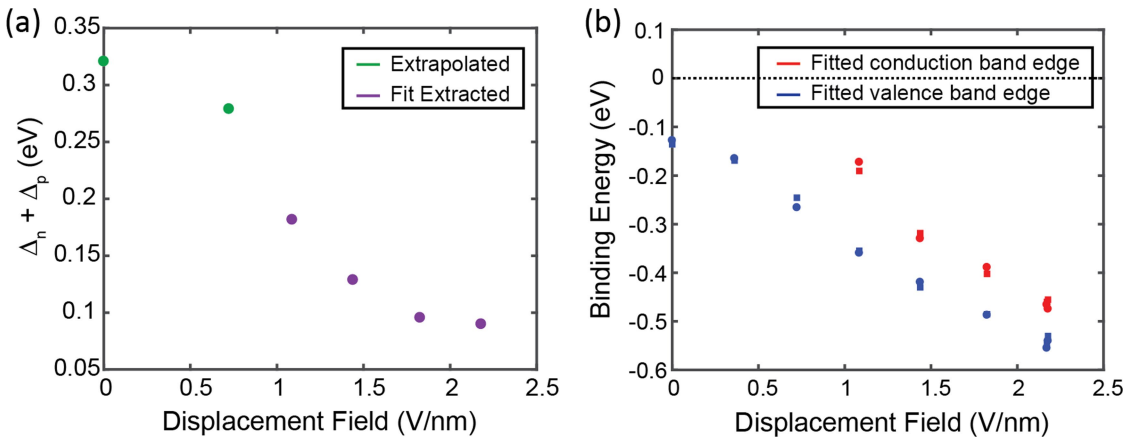

Extended Data Fig. 7 | Electric displacement field-dependence of topological insulator ML/BL Na_3Bi bands near E_F. a, The sum of Δ parameters from the best fit of equation (5) to ARPES dispersion versus applied electric displacement field. Both $\Delta_{n,p}$ are directly calculated from the high-field (purple) measurements, however in low-field (green) measurements, E_F is not sufficiently shifted for the electron dispersion to be clearly resolved. Here we have used the ratio $(\Delta_p + \Delta_n)/\Delta_p \approx 1.4$ measured from the purple points to extrapolate Δ_n for undosed film. **b**, The valence edge (blue) and conduction edge (red) calculated from the fitted ARPES dispersion are shown for two high-symmetry directions: circles for K–Γ–K and squares for M–Γ–M.

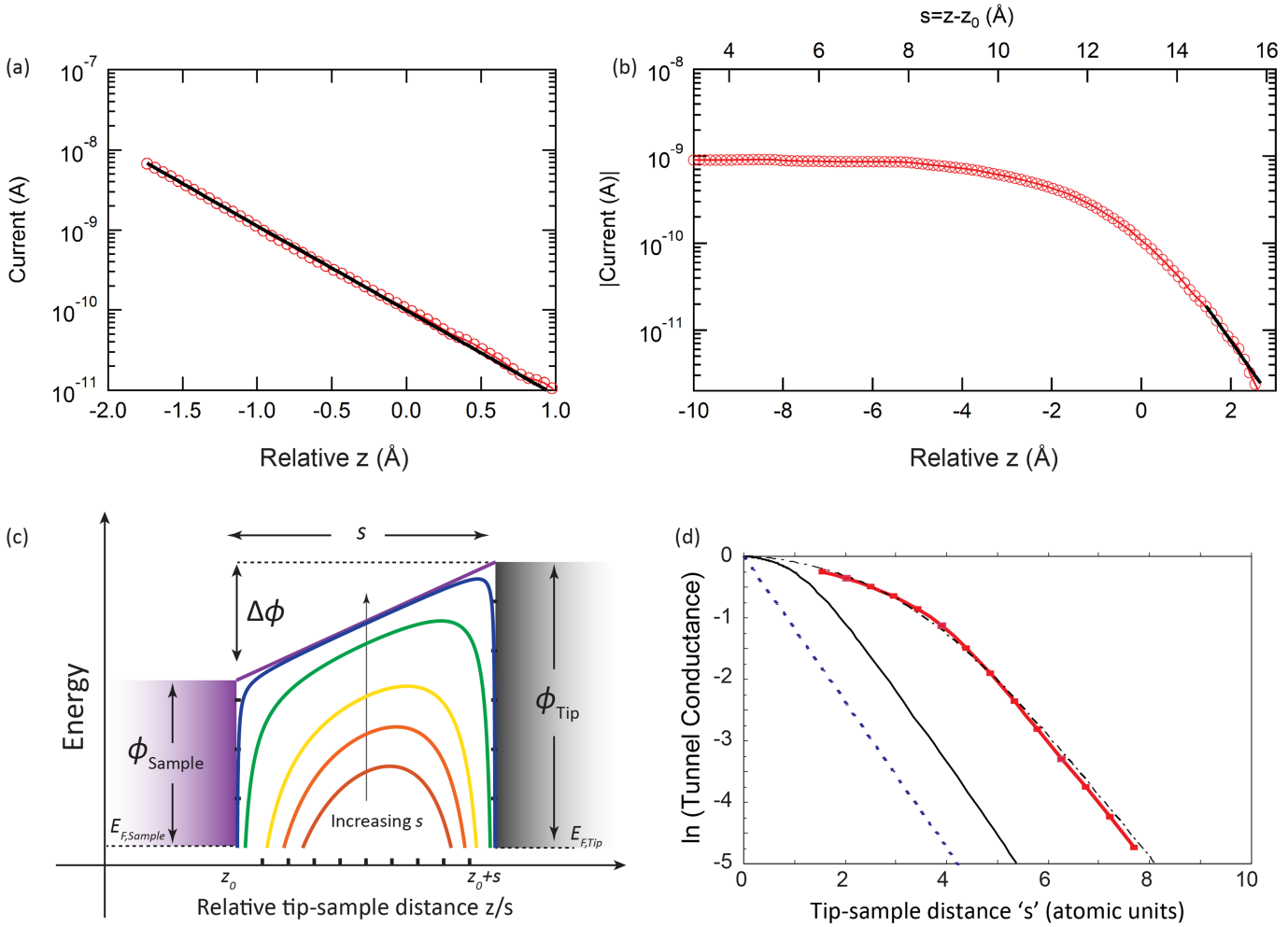

Extended Data Fig. 8 | Electric-field calculations from STM. **a**, **b**, Tunnelling current as a function of relative tip–sample distance z for **a**, Au(111) (bias +500 mV), and **b**, thin film Na_3Bi (bias −300 mV). The top axis in **b** represents the total distance, s, between tip and sample determined as described in Methods section 'Calculating tip–sample separation and electric field'. The black lines in **a** and **b** are exponential fits. **c**, Energy-level schematic illustrating the effects of an image potential on the (purple trapezoidal) junction barrier, where s is the tip–sample distance, and ϕ_{Sample} and ϕ_{Tip} are the work function of the sample and tip, respectively. Progression from blue, green, yellow, orange and red curves indicates modification of the apparent barrier height due to the imaging potential at decreasing tip–sample distances s. **d**, $\ln(I(s)/I_0)$ shown as a function of distance for a square barrier model (blue dashed line), for DFT-LDA (black full line), for the image potential model (black dashed-dotted), and for the local orbital basis model (red line). Data are taken from figure 10 of ref. [41].

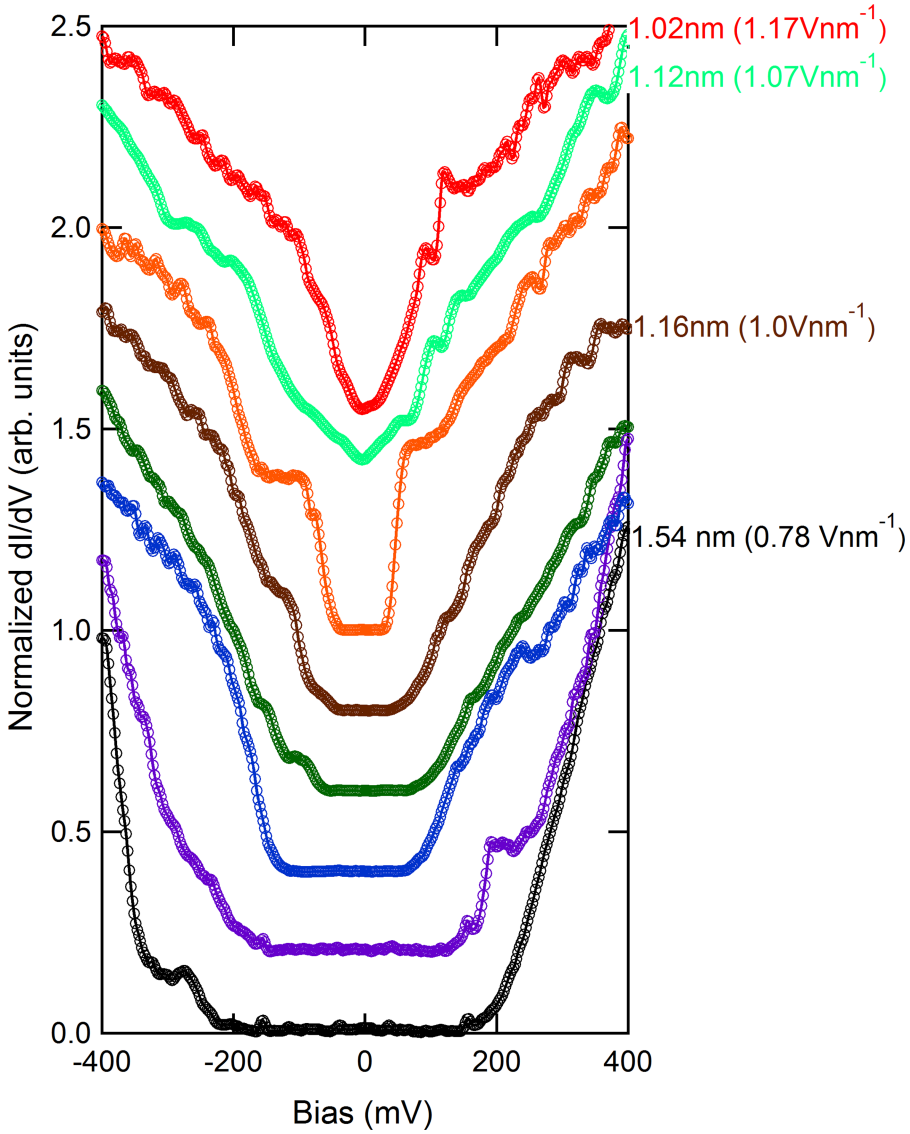

Extended Data Fig. 9 | Scanning tunnelling spectra of ML Na_3Bi. Shown are individual dI/dV spectra taken on ML Na_3Bi at different tip–sample separations (electric field) (shown at right). The spectra have been normalized and offset for clarity.

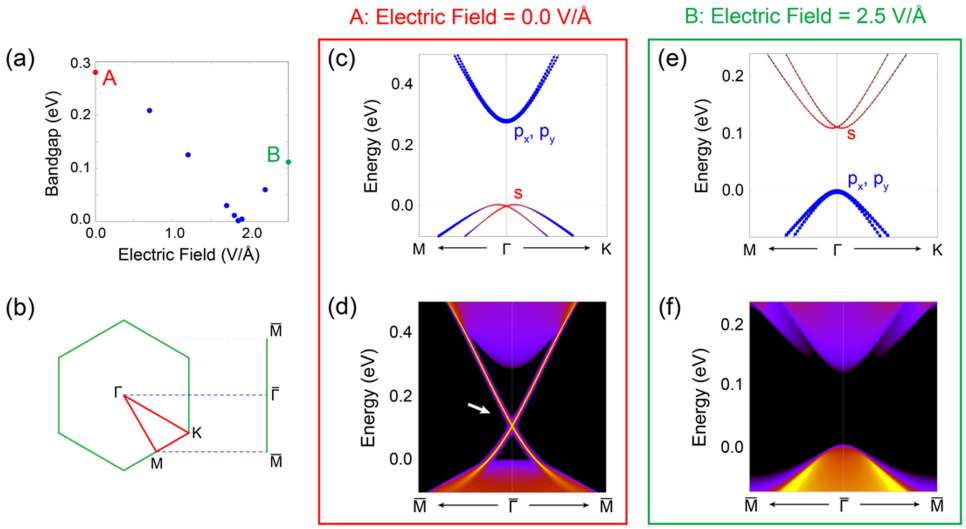

Extended Data Fig. 10 | DFT calculations of Na_3Bi layers with electric field. a, Calculated bandgap variation as a function of electric field for ML Na_3Bi with an Na(2) vacancy. The gap closes and reopens at about 1.85 V $Å^{-1}$. **b**, 2D Brillouin zone and the projected 1D boundary Brillouin zone. **c**–**f**, Orbital-resolved band structures and edge spectra for ML Na_3Bi at electric fields of 0.0 V $Å^{-1}$ (**c**, **d**) and 2.5 V $Å^{-1}$ (**e**, **f**), which are marked by points A and B in **a**. **c**, Orbital-resolved band structures with SOC in the absence of electric field (the energy zero is set to be at the valence band maximum at the Γ point). The red dots represent the contribution from the Na *s* and Bi *s* atomic orbitals, and the blue dots represent the contribution from the Bi p_x/p_y atomic orbitals. A band inversion is observed at the Γ point induced by SOC, indicating that ML Na_3Bi is a non-trivial 2D topological insulator. **d**, Projected edge spectrum (edge along the [010] direction) in the absence of electric field, showing topological edge states. Panels **e** and **f** show the corresponding results at an electric field of 2.5 V $Å^{-1}$. In **e**, the band ordering at Γ is inverted compared to **c**, indicating a topological phase transition to a trivial insulator phase. This is confirmed by the disappearance of topological edge states as shown in **f**.

(a)

ML Na_3Bi	Point Group	Crystalline Symmetries				
		C_{3z}	C_{2x}	M_{xy}	S_{3z}	M_{xz}
Pristine	D_{3h}	✓	✓	✓	✓	✓
E_z	C_{3v}	✓	✗	✗	✗	✓
Na(2) vacancy	C_{3v}	✓	✗	✗	✗	✓

(b)

BL Na_3Bi	Point Group					
		C_{3z}	C_{2x}	I	S_{6z}	M_{yz}
Pristine	D_{3d}	✓	✓	✓	✓	✓
E_z	C_{3v}	✓	✗	✗	✗	✓
Na(2) vacancy	C_{3v}	✓	✗	✗	✗	✓

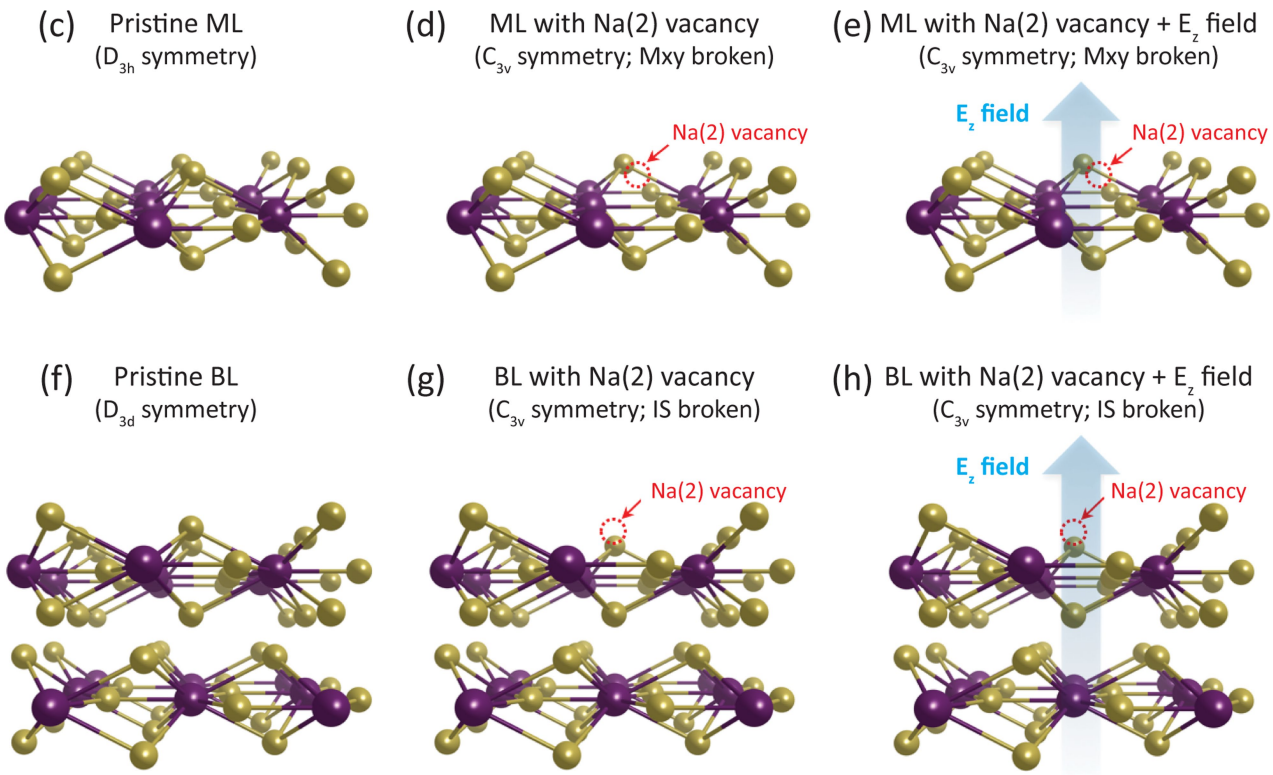

Extended Data Fig. 11 | Crystal structure and symmetries of ML and BL Na_3Bi. a, **b**, Tables showing the point group (PG) symmetries for ML and BL Na_3Bi, respectively. The second and third rows of each table indicate the effects of electric field (E_z) and an Na(2) vacancy, respectively. We note that at zero electric field both pristine and Na(2) vacancy ML and BL Na_3Bi are 2D QSH insulators, with topological index $\upsilon \in \mathbb{Z}_2 = 1$. **c**–**h**, Crystal structure of Na_3Bi as a result of an Na(2) vacancy and electric field. **c**, **f**, Pristine ML (**c**) and BL (**f**) Na_3Bi; **d**, **g**, ML (**d**) and BL (**g**) Na_3Bi each with an Na surface vacancy; **e**, **h**, ML (**e**) and BL (**h**) Na_3Bi with Na surface vacancy plus electric field applied perpendicular to the sample.